Network state-dependent inhibition of identified hippocampal CA3 axo-axonic cells *in vivo*

Tim J Viney[1,3], Balint Lasztoczi[1–3], Linda Katona[1,3], Michael G Crump[1,3], John J Tukker[1], Thomas Klausberger[1,2] & Peter Somogyi[1,2]

Hippocampal sharp waves are population discharges initiated by an unknown mechanism in pyramidal cell networks of CA3. Axo-axonic cells (AACs) regulate action potential generation through GABAergic synapses on the axon initial segment. We found that CA3 AACs in anesthetized rats and AACs in freely moving rats stopped firing during sharp waves, when pyramidal cells fire most. AACs fired strongly and rhythmically around the peak of theta oscillations, when pyramidal cells fire at low probability. Distinguishing AACs from other parvalbumin-expressing interneurons by their lack of detectable SATB1 transcription factor immunoreactivity, we discovered a somatic GABAergic input originating from the medial septum that preferentially targets AACs. We recorded septo-hippocampal GABAergic cells that were activated during hippocampal sharp waves and projected to CA3. We hypothesize that inhibition of AACs, and the resulting subcellular redistribution of inhibition from the axon initial segment to other pyramidal cell domains, is a necessary condition for the emergence of sharp waves promoting memory consolidation.

During slow wave sleep (SWS), quiet wakefulness and consummatory behavior, large-amplitude, 30–120-ms-duration 'sharp wave' voltage deflections have been observed in extracellular recordings throughout the mammalian hippocampal formation[1], which occur simultaneously with 130–230 Hz 'ripples' most pronounced in stratum pyramidale (sPyr) of CA1 (refs. 2,3). These sharp wave–ripple complexes (SWRs) are required for memory consolidation[4] and have been postulated to originate from groups of pyramidal neurons in CA3 participating in a synchronous 'population burst', which is transmitted to the downstream CA1 region via Schaffer collaterals[5]. A proposed mechanism for SWR initiation is through disinhibition of pyramidal cells via dynamic state-dependent interactions between GABAergic neurons and glutamatergic inputs[1]. Indeed, *in vivo* recordings show that some unidentified interneurons decrease and others increase their firing during SWRs[5,6]. Interneurons innervate different subcellular domains of pyramidal neurons, which in dorsal CA1 correlate with their firing patterns during, for example, SWRs[7]. Furthermore, cell type–specific spatiotemporal activity also depends on extrahippocampal inputs from structures such as the medial septum[8], raphe nuclei and entorhinal cortex[9]. Therefore, it is necessary to define the temporal contribution of distinct cell types that may influence or regulate SWR generation.

One group of hippocampal interneurons expresses the calcium-binding protein parvalbumin. Within this group in CA1, bistratified cells target pyramidal cell dendrites in stratum oriens (sOri) and stratum radiatum (sRad), basket cells target pyramidal cell somata and proximal dendrites, and AACs exclusively target the pyramidal cell axon initial segment (AIS). This latter, enigmatic GABAergic interneuron was discovered by János Szentágothai (1912–1994) as the chandelier cell in the neocortex[10], which he later called the

axo-axonal cell when its synaptic target, the AIS, was identified[11]. In marked contrast to parvalbumin-expressing bistratified and basket cells, CA1 AACs do not fire during SWRs[12,13]. This may enable the recruitment of CA1 pyramidal cells during SWRs, as this cell type is ideally placed to regulate pyramidal cell firing. However, SWRs are generated in the upstream CA3 region[5], where the firing activity of AACs *in vivo* is unknown.

RESULTS
Identification of hippocampal AACs
To assess the contributions of AACs to the hippocampal network, we recorded the activity of single interneurons in both urethane-anesthetized and freely moving rats, followed by juxtacellular labeling (**Fig. 1** and **Supplementary Fig. 1**). We identified nine AACs (from nine rats) on the basis of the presence of radial rows of boutons (cartridges) around the sPyr-sOri border (**Fig. 1a,c**)[14]. Dendrites of seven AACs crossed stratum lucidum (sLuc), demonstrating the cells' location in CA3. The dendrites were radially distributed across all strata, with a broad tuft aligned with the entorhinal cortical input in stratum lacunosum-moleculare (sLacMol) ($n = 8$ AACs, **Fig. 1a**), representing $34.7 \pm 7.6\%$ (mean ± s.d.) of the total dendritic length ($n = 3$ AACs, **Fig. 1a,b**). A smaller proportion was found in sRad ($11.8 \pm 8.3\%$) and only minor proportions in sLuc ($1.9 \pm 0.4\%$) and sPyr ($4.9 \pm 2.4\%$). The highest proportion of dendrites was in sOri and the alveus ($46.7 \pm 6.7\%$). Thus, CA3 AAC dendrites are aligned with pyramidal cell dendrites[15]. One CA3 AAC had dendrites and axon in CA2 (**Fig. 2a**). From two AACs recorded in freely moving rats, one was located in CA2 and had axon innervating both CA2 and CA3 but not CA1; the other was located in CA1 and innervated CA1 pyramidal cells.

Figure 1 Identified CA3 AACs fire less during SWR events *in vivo*. (**a**) Full reconstruction of somata and dendrites of three identified AACs (cells B10a, J54a and B45a, from 11, 9 and 11 70-μm-thick sections of rats B10, J54 and B45, respectively), color-coded for layers (sOri includes alveus). The axon of B45a (black) is shown from one section. (**b**) Distribution of dendritic lengths, with total length shown at top. (**c**) Light microscopic images of B45a axon cartridges, identifying the cell type. (**d**) Somatic neurobiotin labeling of B45a (left, asterisk) and SATB1 immunoreactivity (blue, right) in the nuclei of two unidentified cells (arrows); the AAC is immunonegative (asterisk). (**e**) A neurobiotin-labeled proximal dendrite of B45a (left, arrow) is immunopositive for parvalbumin (PV) and ErbB4. (**f**,**g**) Firing patterns of cell B45a during SWRs (**f**) and theta oscillations (**g**). Top to bottom in **f**: LFP recorded in CA1 sPyr, first unprocessed and then band-pass filtered at 90–200 Hz; action potentials of the cell (spikes); LFP simultaneously recorded by a tetrode in sPyr of CA3b-c, first band-pass filtered and then unprocessed. Detected ripples are shown in red. Firing of the cell is suppressed during SWRs in CA3 and CA1. Top to bottom in **g**: CA1 LFP; spikes; CA3 LFP from the tetrode. The cell fires rhythmically at the peak of CA1 theta oscillations. Theta oscillations in CA3 are coherent with those in CA1. Scale bars (μm): **a**, 100; **c**,**e**, 10; **d**, 20. Panel **e**, maximum intensity projection of 13 optical sections (5.1-μm-thick z-stack); **d**, two 0.33-μm-thick optical sections from two different depths in the same z-stack.
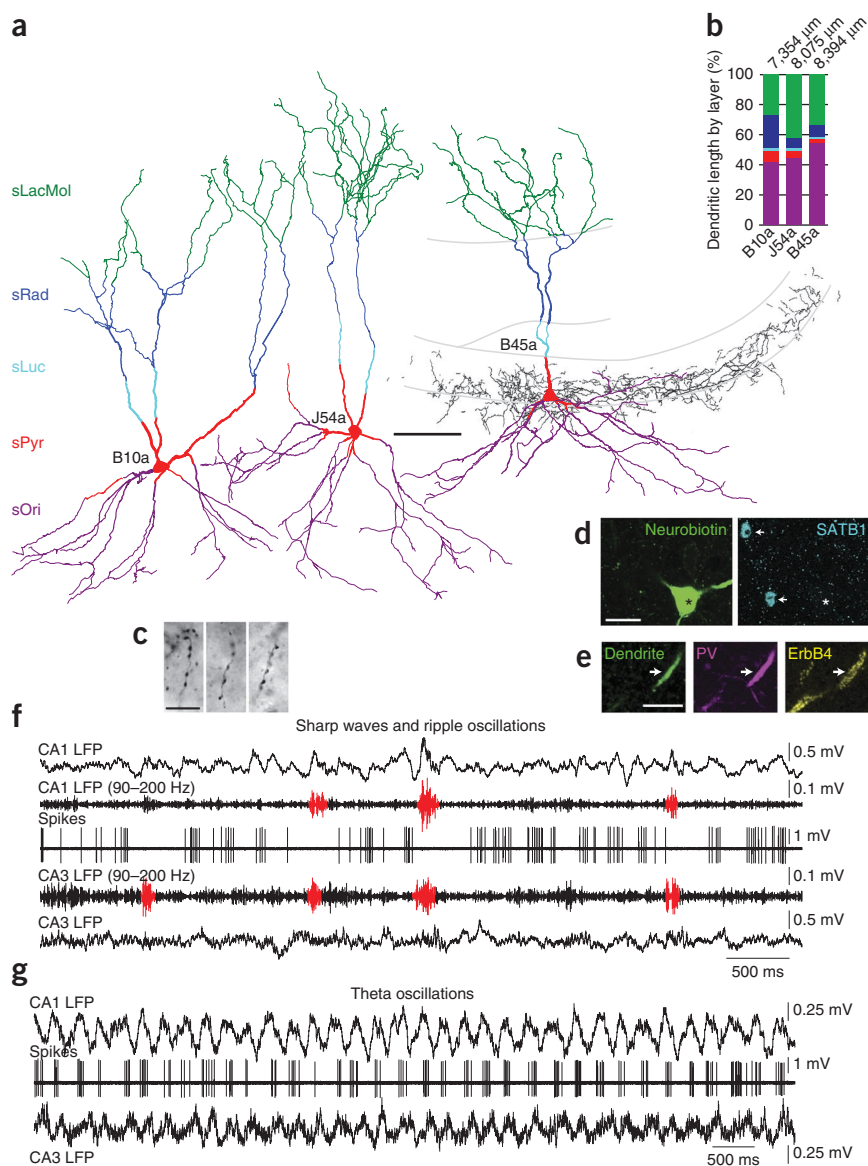
Next we tested the molecular profiles, postsynaptic targets and firing patterns of AACs (**Table 1**). All AACs were immunoreactive for parvalbumin (PV+) ($n = 9$ of 9 cells examined), and their somatodendritic membrane expressed small puncta and large patches of ErbB4 (ref. 16) ($n = 5$ of 5 cells) (**Fig. 1d**,**e**). In contrast to other identified PV+ cells, such as CA1 bistratified cells and oriens lacunosum-moleculare cells[12,13], AACs lacked detectable immunoreactivity for neuropeptide Y (NPY) and somatostatin (SOM) ($n = 0$ of 2 for both molecules) and were also immunonegative for neuronal calcium-binding protein 1 (NECAB1)[17] ($n = 0$ of 4 tested cells).

Testing for postsynaptic targets using ankyrin G, a marker for the AIS[18], showed that AAC boutons targeted the AISs of pyramidal cells[14] ($n = 3$ cells, **Fig. 2b**). These AISs were covered by vesicular GABA transporter (VGAT)-immunoreactive boutons, the labeled AAC terminals being a subset of these (**Fig. 2b**). Electron microscopy confirmed that these sites were GABAergic synapses[14] with membrane specialization (100% targeted AISs[19]; $n = 7$, 13, 11, 14, 10 and 9 synapses for cells B10a, LK24g, TV34n, B45a, B44a and B53b, respectively; **Fig. 2c** and **Supplementary Figs. 1a** and **2**). Thus, CA3 AACs release GABA selectively on the AIS.

Firing patterns of AACs during sharp waves

To explore the firing patterns of CA3 AACs, we identified SWRs (90–200 Hz oscillations) and theta oscillations (3–6 Hz) in local field potentials (LFPs) recorded in both CA3 and CA1 of anesthetized

rats (**Figs. 1f**,**g** and **2a**). Transitions between different states occurred spontaneously or were promoted by administration of anesthetics (SWRs and non-theta states) or a tail pinch (theta). Coincident with the occurrence of SWRs, firing of AACs often ceased completely, despite firing heavily before and after (**Fig. 1f**). The number of action potentials fired by individual CA3 AACs was less during SWRs than expected from their firing in a ±10-s window around the SWRs (SWRs versus 'peri-SWRs' significant at $\alpha = 0.05$ with Mann-Whitney U-test in 3 of 3 and 5 of 5 cells for CA3 and CA1 SWRs, respectively; **Fig. 2e** and **Table 1**). Mean (± s.d.) firing rates dropped from 24.6 ± 4.0 Hz and 22.8 ± 3.1 Hz peri-SWR to 4.4 ± 3.7 Hz and 4.8 ± 3.5 Hz during SWRs ($P = 0.039$ and 6×10^{-4}; $t_2 = 4.9$ and $t_4 = 9.7$; $n = 3$ cells and 5 cells, for SWRs detected in CA3 and CA1, respectively; paired Student's t-tests; **Fig. 2e**). We detected significant variation in the mean firing rate of AACs as a function of normalized SWR time ($P = 4 \times 10^{-8}$ and 6×10^{-13}; $F_{31,64} = 4.88$ and $F_{31,128} = 5.74$; $n = 3$ and 5 cells for CA3 and CA1 SWRs, respectively; one-way ANOVA), with a significant reduction in the rate associated with SWR occurrence (Tukey's *post hoc* multiple comparisons test; **Fig. 2d**). Consistent with the generation of SWRs in CA3 (ref. 5), we found that $30 \pm 10\%$

Figure 2 GABAergic input to CA3 pyramidal cell AISs is withdrawn during sharp waves *in vivo*. (**a**) Locations of CA1 electrodes (black asterisk, rats B44, B10, B45, J67, B62 and B53; brown asterisk, rat J54), tetrode tips (color-coded open circles) and somata of AACs (color-coded filled circles). TV34n and LK24g are from drug-free, freely moving rats. (**b**,**c**) Examples of AACs (**b**, J67d; **c**, B10a and LK24g) innervating pyramidal cell AISs. (**b**) Neurobiotin-filled axonal boutons (green, arrows), immunoreactive for VGAT (yellow, right) are apposed to AISs immunolabeled for ankyrin G (magenta). (**c**) Electron micrographs of neurobiotin-labeled (horseradish peroxidase end product) boutons (B) of B10a (left) and LK24g (right) making type II synapses (filled arrows) with AISs, identified by membrane undercoating (asterisk) and linked microtubules (arrowhead). An unlabeled bouton also makes a synapse (open arrow). SV, synaptic vesicles. (**d**) Variation of firing rate of AACs before, during (gray box) and after SWRs detected in CA3 (top) or CA1 (middle; lines, individual cells; gray bars, mean ± s.d.; asterisks significant at $\alpha = 0.05$ by Tukey's *post hoc* comparisons). Bottom: firing rates for identified AACs TV34n and LK24g recorded in drug-free rats; SWRs detected from the electrode recording the cell. (**e**) Overall firing rates during and outside SWRs (peri-SWR) detected in CA3 or CA1. Individual cells are color-coded as in **a** (mean ± s.d. in black; asterisks, significant at $\alpha = 0.05$ with paired *t*-test; $P = 0.039$ and 6×10^{-4} for SWRs detected in CA3 and CA1, respectively). (**f**) Firing of LK24g during sleep. Top to bottom traces: Electroencephalogram (EEG) in frontal cortex; band-pass filtered (130–230 Hz) LFP at the recording site of the cell (CA2), SWRs in red; action potentials; LFP. Scale bars: **a**, 1 mm; **b**, 5 μm; **c**, 0.5 μm. Panel **b**, maximum intensity projection of 9 optical sections (2.8-μm-thick *z*-stack). DG, dentate gyrus.
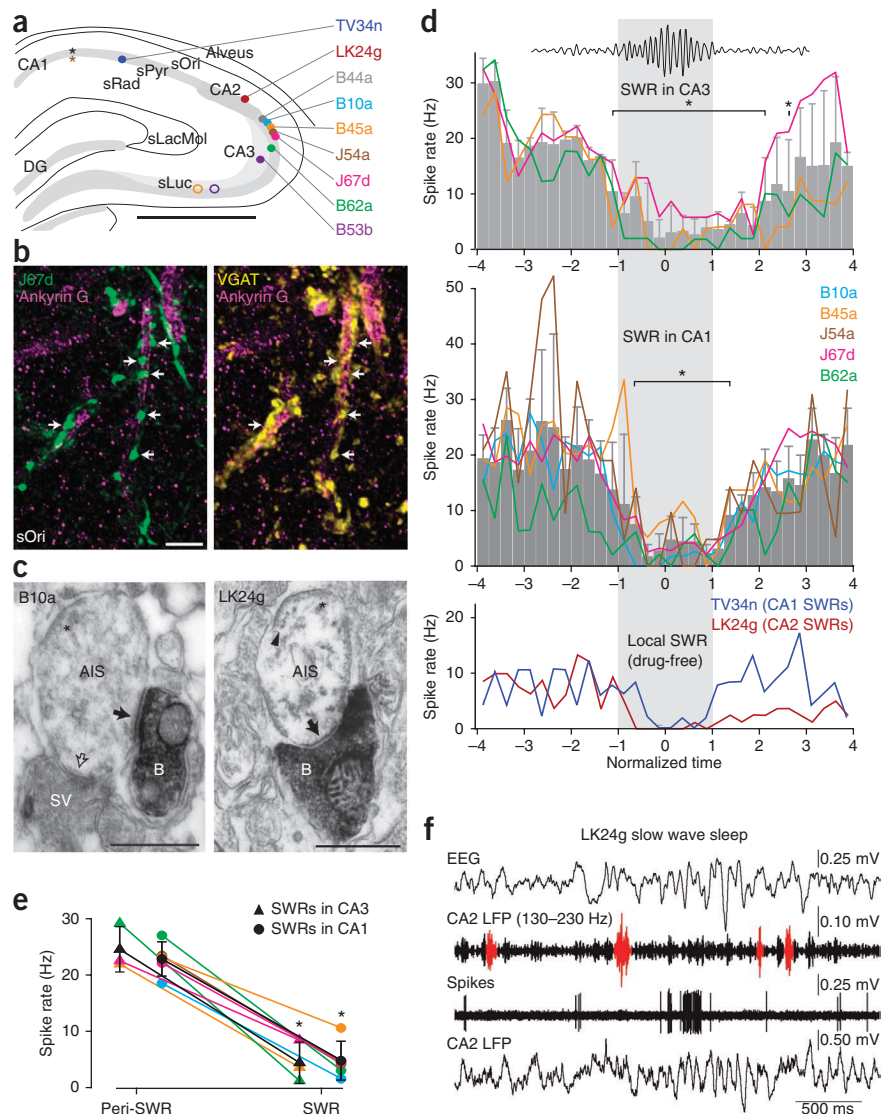
(mean ± s.d.) of detected SWRs occurred coincidentally in CA3 and downstream CA1 (*n* = 3 experiments from 3 rats). Some SWRs (27 ± 4.5%) detected by the CA3 electrode did not recruit the CA1 area at the CA1 electrode site; others detected only in CA1 (43 ± 14%) could have originated from sites other than that of the CA3 electrode. Suppression of CA3 AAC firing was similar irrespective of where the SWRs were detected (reduction to 19 ± 14% versus 21 ± 13% during SWRs in CA3 and CA1, *n* = 3 and 5 cells, respectively; *P* = 0.9; $t_6 = 0.13$; two-sample Student's *t*-test; **Fig. 2e**). In both areas, small increases in the power of 90–200 Hz oscillations, below the threshold of SWR detection and possibly reflecting distant, localized SWRs, were often associated with AAC silencing (**Fig. 1f**), suggesting that the suppression of AACs occurs on most SWRs.

To test whether the observed suppression of firing during SWRs could be detected in animals without anesthesia, we examined firing patterns of identified AACs recorded in drug-free, freely moving rats[20]. During SWS and quiet wakefulness, we observed a reduction in AAC firing during local SWRs (**Fig. 2f** and **Supplementary Fig. 1b**; 130–230 Hz oscillations). Identified AACs in both CA2 and CA1 significantly decreased their firing rate during SWRs compared to peri-SWR periods (CA2, cell LK24g: 0.72 Hz versus 8.8 Hz, *P* = 6 × 10⁻⁷,

n = 112 SWRs; CA1, cell TV34n: 2.4 Hz versus 6.9 Hz, *P* = 0.026, *n* = 61 SWRs; Mann-Whitney *U*-test; **Fig. 2d** and **Table 1**). The overall firing rate was very low during resting states, when SWRs occurred (**Supplementary Fig. 3** and **Table 1**). Occasionally, AACs fired in bursts (**Fig. 2f**) uncorrelated to SWRs. We conclude that AACs are inhibited during SWRs under drug-free conditions also.

Theta- and gamma-modulated firing of AACs

During theta oscillations under anesthesia, CA3 AACs fired rhythmically at 28.8 ± 4.2 Hz (mean ± s.d.; *n* = 5 cells from 5 rats), with six to eight action potentials per cycle (**Fig. 1g** and **Table 1**). Firing of AACs was lowest around theta troughs detected either locally in CA3 or in CA1 (**Figs. 2a** and **3a**), suggesting a reduction in GABAergic input to CA3 AISs at this phase (**Fig. 2b,c**). Correspondingly, the preferred theta phase of firing was close to the peak, at 146° ± 28.1° for CA3 theta oscillations (circular mean ± circular s.d.; *n* = 6 cells; **Fig. 3a** and **Table 1**) and at 183° ± 21.7° for CA1 theta (*n* = 5 cells; only CA1 electrode in sPyr included; all AACs significant at $\alpha = 0.05$, Rayleigh test; **Fig. 3a** and **Table 1**). Consistent with the strong theta modulation of AACs, the mean vector lengths were similarly high (0.44 ± 0.07 in CA3 versus 0.45 ± 0.06 in CA1, mean ± s.d.; *P* = 0.48, $t_5 = 0.75$, *n* = 6,

Table 1 Properties of identified AACs

Cell	B44a[a]	B10a	B45a	J54a[b]	J67d	B62a	B53b[c]	LK24g[d]	TV34n[d,e]
Region	CA3	CA3	CA3	CA3	CA3	CA3	CA3	CA2	CA1
Immunohistochemistry, histology									
Parvalbumin	+ D	+ D	+ D	+ D	+ D	+ A	+ DS	+ D	+ A
SATB1	− N		− N		− N	− N	− N	− N	
ErbB4	+ D		+ D		+ D	+ DS	+ DS		
NECAB 1	− D		− D		− D		− D		
Somatostatin				− S		− S			
Neuropeptide Y	− S					− S			
VGAT	+ A				+ A		+ A		
GABAergic input (VGAT)		+ D		+ D	+ D				
Calbindin			− D		− AD				
Targets AIS (ankyrin G)	+ A				+ A		+ A		
Targets AIS (EM)	+ (10/10)	+ (7/7)	+ (14/14)				+ (9/9)	+ (13/13)	+ (11/11)
In vivo firing patterns									
CA2/3 SWRs									
Rate during SWRs (Hz)	NA	NA	3.5	NA	8.4	1.2	NA	0.7	NA
Rate peri-SWR (Hz)	NA	NA	21.9	NA	22.5	29.2	NA	8.8	NA
U-test P value	NA	NA	2×10^{-6}	NA	10^{-10}	5×10^{-19}	NA	6×10^{-7}	NA
Total n SWRs (active n)	NA	NA	23 (4)	NA	80 (28)	50 (3)	NA	112 (5)	NA
CA1 SWRs									
Rate during SWRs (Hz)	NA	1.5	10.6	4.1	4.5	3.0	2.6	NA	2.4
Rate peri-SWR (Hz)	NA	18.5	23.1	23.5	22.1	27	8.3	NA	6.9
U-test P value	NA	4×10^{-32}	5×10^{-5}	3×10^{-6}	6×10^{-31}	10^{-13}	0.250	NA	0.026
Total n SWRs (active n)	NA	106 (11)	28 (12)	20 (6)	147 (35)	49 (7)	7 (1)	NA	61 (7)
Non-theta firing rate (Hz)	NA	19.4[f]	NR	NR	19.7[f]	27.9	7.63		
Theta firing rate (Hz)	NA	25.9	29.0	32.1	23.5	33.4	3.2	20.4	17.5
Head movement rate (Hz)								17.1	24.4
Slow-wave sleep rate (Hz)								8.2	6.0
Quiet wakefulness rate (Hz)								7.2	8.8
Theta coupling									
Mean phase CA2/3 (°)	NA	142.2	152.7	153.6	193.4	94.8	138.4	190.6	NA
Mean vector length CA2/3	NA	0.39	0.51	0.38	0.44	0.38	0.54	0.48	NA
Rayleigh test P value	NA	$<10^{-100}$	$<10^{-100}$	$<10^{-100}$	$<10^{-100}$	10^{-29}	3×10^{-7}	$<10^{-100}$	NA
Mean phase CA1 (°)	NA	169.7	194.9	247.3	218.4	154.4	178.7	NA	225.3
Mean vector length CA1	NA	0.43	0.54	0.36	0.43	0.45	0.51	NA	0.42
Rayleigh test P value	NA	$<10^{-100}$	$<10^{-100}$	$<10^{-100}$	$<10^{-100}$	7×10^{-21}	4×10^{-8}	NA	6×10^{-14}
Total n spikes	NA	19,195	20,706	3,880	1,691	308	54	1,897	164

Positive and negative immunoreactivity or connectivity indicated by + and −, respectively. Measurement location: S, soma; N, nucleus; D, dendrites; A, axons; NA, not available; NR, not recorded. EM, electron microscopic evidence. U-test (Mann-Whitney U comparison) P values significantly different from peri-SWR at $\alpha = 0.05$. Rayleigh test P values significantly different from a uniform phase distribution of spikes at $\alpha = 0.05$.
[a]The recorded firing patterns could not be assigned to a cell because two labeled cells were recovered. [b]CA1 electrode LFP recorded in sRad, accounting for a CA1 theta phase shift. [c]Cell recorded under unusually deep anesthesia. [d]Recorded in drug-free freely moving rats. [e]The soma and dendrites were lost during labeling. [f]Significantly different from the theta firing rate (Mann-Whitney U-test at $\alpha = 0.05$).

paired t-test). In freely moving rats, theta oscillations were observed during head movements and postural shifts; the animals remained in the same location throughout the recording period. Firing of AACs during movement occurred at a high rate and was rhythmic but intermittent (**Fig. 3b,c**, **Supplementary Figs. 1c** and **3a,b**, and **Table 1**). Firing rates and consequent GABA release on CA2 and CA3 pyramidal cells (LK24g) and on CA1 pyramidal cells (TV34n) were lowest close to theta troughs, with preferred firing phases of 191° and 225°, respectively (phase distributions significantly different from uniform at $\alpha = 0.05$, Rayleigh tests; **Fig. 3b** and **Table 1**). Notably, AACs fired at a similar rate to CA1 PV^{+} basket cells (PVBCs)[20] during theta oscillations in drug-free rats (**Supplementary Fig. 3a,c**) but were more strongly theta-modulated (AAC vector lengths: 0.48 in CA2, LK24g; 0.42 in CA1, TV34n; mean of mean vector lengths ± s.d. for 5 PVBCs[20], 0.22 ± 0.06). Differences in firing of AACs and PVBCs were evident across behavioral states (**Supplementary Fig. 3b,d**).

Identified CA3 AACs are not coupled to kainate-induced gamma oscillations *in vitro*[21], whereas CA1 AACs are coupled locally *in vivo*[22]. We have examined the relationship between AAC firing and 15–100 Hz LFP oscillations under anesthesia. We observed coupling (at $\alpha = 0.01$, Rayleigh test; $n = 33,003, 30,870, 9,633, 14,673, 26,474$ and

34,760 spikes for cells B10a, B45a, B53b, B62a, J54a and J67d, respectively) to CA1 gamma oscillations (mean vector length (reflecting phase coupling strength) $r = 0.06 \pm 0.04$ at the frequency of strongest coupling, 59 ± 12 Hz; mean ± s.d.; $n = 6$ cells; **Fig. 3f**) and relative to CA3 gamma oscillations (**Fig. 3d–f**) from either the local electrode ($r = 0.16 \pm 0.09$ at the strongest coupling frequency, 71 ± 24 Hz; $n = 6$; $P = 0.066$, $t_5 = 2.35$; for r compared to CA1, paired t-test; **Fig. 3f**) or a nearby tetrode in CA3 sPyr ($n = 2$; **Fig. 3d–f**). Variability in firing phase may have resulted from the variable position of the electrode tips (compare **Figs. 2a** and **3f**). Nevertheless, CA3 AACs show significant phase-coupling to gamma oscillations, comparable in strength and phase to those of CA3 pyramidal cells[23] and PVBCs[24].

Identification of inputs to AAC dendrites

Next we investigated synaptic inputs to AAC dendrites that could shape their firing patterns. Immunoreactivity for the presynaptic active-zone protein bassoon[25] showed that $9.7 \pm 0.7\%$ (mean ± s.d.) of putative synapses colocalized with VGAT puncta ($n = 215$ bassoon puncta, 3 cells from 3 rats; **Fig. 4a**), suggesting a relatively small proportion of GABAergic synapses on dendrites. Electron microscopy confirmed that AAC dendrites receive GABAergic synaptic input

Figure 3 AACs in CA3 fire rhythmically around the peak of theta oscillations and are coupled to gamma oscillations *in vivo*. (**a**) Firing rate of AACs (color-coded) as a function of theta phase (sinusoid shown above) recorded locally in CA3 (top) and at a reference site in CA1 (bottom; black trace is the mean). (**b**) Firing rate versus theta phase (local electrode) for identified AACs recorded from drug-free rats in CA2 (LK24g) and CA1 (TV34n). (**c**) Firing patterns of LK24g during head movement of the rat. Top to bottom traces: electroencephalogram (EEG); action potentials of the cell; LFP revealing rhythmic theta oscillations. (**d**) Modulation of spike timing (cell B45a) by the phase of gamma oscillations from a CA3 tetrode. Left, mean vector length (*r*) as a function of gamma frequency (15–100 Hz, 85 logarithmically equidistant bins). Right, spike count (color-coded) binned as a function of gamma phase (20 bins per cycle) and frequency (15–100 Hz, 85 logarithmically equidistant bins). White line, mean phase spectrum. (**e**) Representative LFP and spikes for the same cell as in **d**. Unprocessed CA3 tetrode LFP (gray), filtered tetrode LFP (gamma, 30–80 Hz, black), spikes (orange). (**f**) Summary of gamma coupling for all cells recorded in anesthetized rats (color code as in **a**; B53b, purple). Position of circle represents the frequency at which the coupling is maximal and the mean phase observed at this frequency. Size of circle represents coupling strength (vector length, *r*) at the same frequency. Filled, open and dashed circles represent AAC coupling to gamma oscillations recorded by CA1 electrode, local CA3 electrode and a tetrode wire in CA3, respectively (for positions, consult **Fig. 2a**).
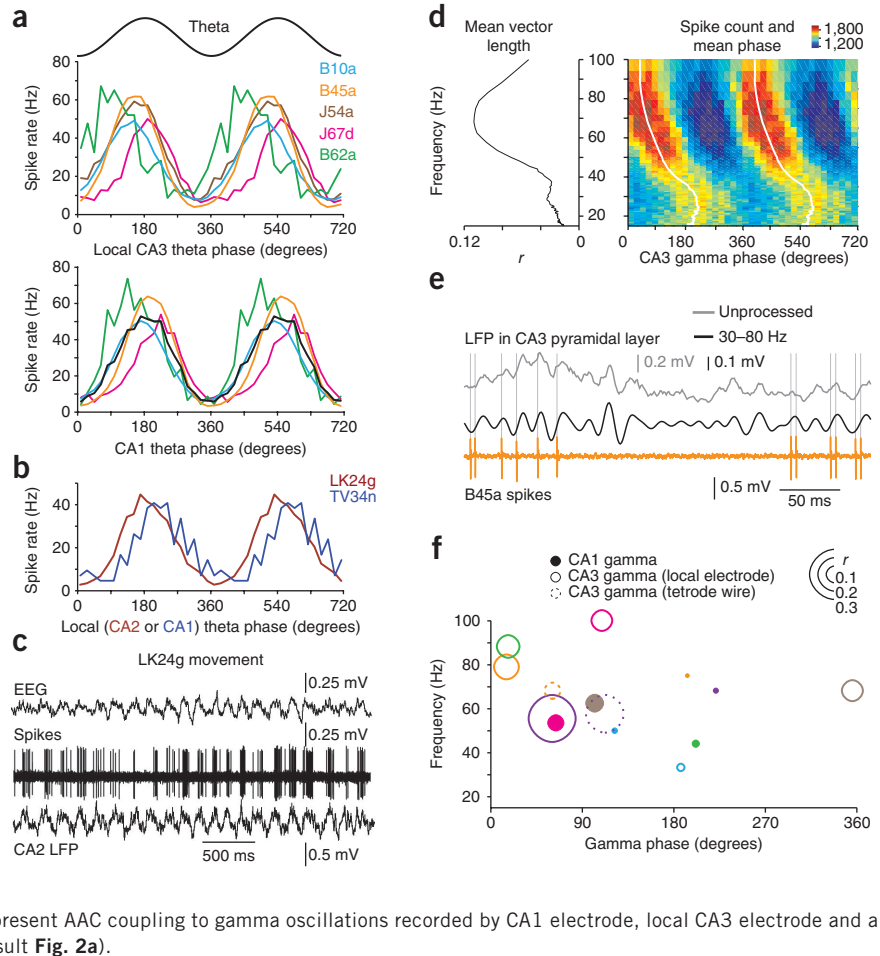
($n = 22$ VGAT$^+$ terminals with synaptic junctions on dendrites of AAC B10a; **Fig. 4b**). These inputs could originate from the medial septum or from hippocampal interneurons. Two molecular markers differentiating the source of GABAergic terminals are parvalbumin and vasoactive intestinal polypeptide[26], but the AAC-dendrite-innervating VGAT$^+$ puncta were immunonegative for both molecules (data not shown).

Large mossy fiber terminals of dentate granule cells target pyramidal cell spines in sLuc, whereas thin filopodial extensions target interneuron dendrites[27]. Surprisingly, we have also found synapses from large mossy fiber terminals on identified AAC dendrites, which also targeted the thorny excrescences of pyramidal cells (**Fig. 4c** and **Supplementary Fig. 4**). Smaller boutons in sLuc, representing the filopodial extensions, also made synapses on AAC dendrites. From a total of 52 (cell B10a) and 82 (cell B45a) synaptic junctions sampled on 2 dendrites of each cell in sLuc, 6 and 3 synapses were made by large mossy fiber terminals, respectively. The metabotropic glutamate receptor type 7b (mGluR7b) is localized to the presynaptic active zone of mossy fiber terminals predominantly in synapses to interneurons[28]. However, mGluR7b-immunoreactive puncta were not found around AAC dendrites, in contrast to adjacent highly decorated unlabeled (neurobiotin-lacking) interneuron dendrites (**Fig. 4d**). These data show that AAC dendrites receive similar mGluR7b-negative glutamatergic granule cell input to that of pyramidal cells[29].

### Immunonegativity for SATB1 identifies PV$^+$ AACs

Specific transcription factors mark neuronal subpopulations. We investigated the immunoreactivity for special AT-rich sequence binding protein 1 (SATB1; **Fig. 5**), which labels unidentified hippocampal interneurons[30]. We found SATB1 immunoreactivity in the nuclei of some PV$^+$ (**Fig. 5a**), NPY$^+$, SOM$^+$, calbindin$^+$, procholecystokinin$^+$ and ErbB4$^+$ interneurons, but not in neurons immunoreactive for neuronal nitric oxide synthase (data not shown). In both CA3 and CA1, some PV$^+$ neurons, among other, SATB1$^+$PV$^+$ double-positive neurons, lacked detectable immunoreactivity for SATB1 (were SATB1$^-$) (**Fig. 5b,c**).

Of PV$^+$ interneuron types with somata in or near sPyr—AACs, basket cells and bistratified cells[31]—only the bistratified cells express SOM and NPY[13]. We detected SATB1 immunoreactivity in all PV$^+$ neurons that were either SOM$^+$, NPY$^+$ or double-positive in sPyr of both CA3 ($n = 25$ of 25 cells; **Fig. 5b**) and CA1 ($n = 46$ of 46 cells). Of all PV$^+$ somata located in CA3 sPyr ($n = 236$ cells), $10.7 \pm 4.4\%$ (mean $\pm$ s.e.m. in 4 sections from 3 rats) were immunoreactive for both SATB1 and either SOM or NPY or both, $56.9 \pm 7.7\%$ were immunoreactive for SATB1 alone and $32.5 \pm 7.6\%$ showed immunoreactivity for neither SATB1 nor SOM or NPY (**Fig. 5e**). All PV$^+$ neurons were positive for the GABA$_A$ receptor $\alpha 1$ subunit[31] (**Fig. 5b–d**). Similar proportions of PV$^+$ somata were observed in CA1 ($13.7 \pm 4.2\%$ SATB1$^+$SOM$^+$, SATB1$^+$NPY$^+$ or SATB1$^+$SOM$^+$NPY$^+$; $59.7 \pm 3.3\%$ SATB1$^+$ only; $26.5 \pm 3.8\%$ SATB1$^-$; $n = 362$ cells, 4 sections, 3 rats; **Fig. 5e**). The proportion of PV$^+$SATB1$^+$ neurons is consistent with previous counts of putative PVBCs[31]. We found similar proportions of PV$^+$ cells in mouse, suggesting that certain mouse PV$^+$ interneurons may be homologous to those characterized in the rat[32] (mouse CA3: $13.5 \pm 3.6\%$ SATB1$^+$SOM$^+$; $59.8 \pm 3.4\%$ SATB1$^+$ only; $26.7 \pm 3.8\%$ SATB1$^-$;

Figure 4 Innervation of AAC dendrites by GABAergic and mossy fiber terminals. (**a**) Synaptic input to an AAC dendrite (asterisk, cell B10a, single optical section) in sOri. Neurobiotin, green; parvalbumin, magenta; bassoon, cyan; VGAT, yellow. A subset of bassoon puncta apposed to the dendrite colocalize VGAT (arrows). (**b**) Electron micrographs of VGAT+ terminals (containing Ni^{2+}-intensified electron-opaque reaction product of horseradish peroxidase) making type II synapses (white arrows; boxed region on right enlarged below) and a VGAT-negative bouton (black arrow) making a type I synapse with a neurobiotin-labeled AAC dendrite (dend, horseradish peroxidase reaction product, B10a, two cross-sections at different levels). (**c**) Electron micrograph of a neurobiotin-labeled AAC dendrite (dend, B10a) receiving synaptic input (white arrows) from three small boutons, and a large mossy fiber bouton (MF) recognized by dense vesicular filling. S, thorny excrescence of CA3 pyramidal cell dendrite. (**d**) Confocal maximum intensity projection (13 optical sections, 4.29-µm-thick z-stack) of mGluR7b immunoreactivity in presynaptic terminals (magenta) and AAC dendrites (arrows; neurobiotin, green; J54a). Asterisk, unlabeled strongly mGluR7b-decorated dendrite. Small green dots, mitochondrial endogenous biotin. Inset, single optical section demonstrating lack of mGluR7b puncta apposed to the labeled AAC dendrite. Two unlabeled mGluR7b-decorated dendrites are on either side. Scale bars (µm): **a**, 2; **b**, 0.5; **c**, 0.5, inset 0.25; **d**, 20, inset 5.
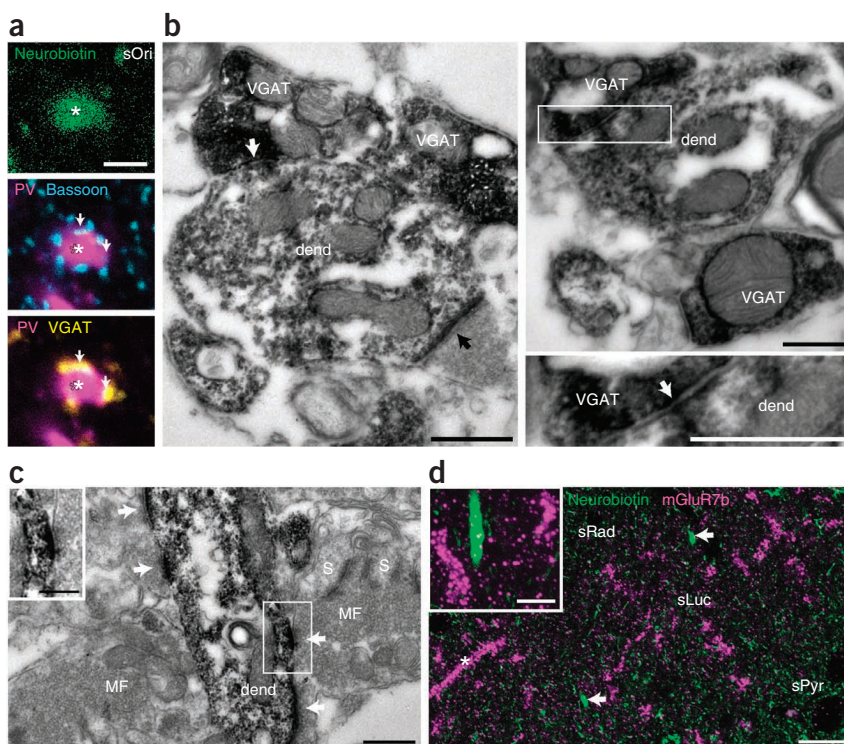
$n = 248$ cells, 4 sections, 3 mice; CA1: $8.5 \pm 4.3\%$ SATB1+SOM+; $69.3 \pm 5.2\%$ SATB1+ only; $22.2 \pm 4.5\%$ SATB1−; $n = 297$ cells, 4 sections, 3 mice; **Fig. 5e**). Of note, we often observed clusters of neurons with a similar molecular profile, such as PV+SATB1+SOM− (**Fig. 5d**) or PV+SATB1−SOM−, suggesting grouping of interneuron types.

To determine whether SATB1 immunoreactivity can be used to differentiate PVBCs from AACs, we tested identified interneurons labeled *in vivo* with neurobiotin. Five of five CA3 and one of one CA2 AACs lacked detectable nuclear SATB1 immunoreactivity (**Figs. 1d** and **5f** and **Table 1**), as did two AACs from intermediate CA1 (TF31a, TF35c). Six of six identified PVBCs in CA1 were SATB1+ (M01b, K03b and B102b; TV08k, K208c and O83f[20]; **Fig. 5f**), as was one PV+SOM+ bistratified cell in CA3 (TV32n). Thus, PV+ interneurons that do not express SATB1 are AACs, representing ~30% of the PV+ population in sPyr of both CA3 and CA1.

Innervation of AACs by the medial septum
Medial septal GABAergic neurons innervate diverse types of hippocampal interneurons[8]. We labeled the axons of medial septal neurons with *Phaseolus vulgaris* leucoagglutinin (PHA-L; $n = 3$ rats; **Fig. 6a**). In the medial septum, we observed clusters of labeled neurons, and axonal targets were consistent with known septal projections[33], including the hippocampus. In a control, PHA-L injected in the lateral septum produced very sparse labeling in the hippocampus.

Septo-hippocampal axons in CA3 and CA1 were of either type I (thick, putatively GABAergic) or type II (thin, putatively cholinergic)[8]. Individual type I axons had boutons apposed to the somata and proximal dendrites of some PV+ neurons but they bypassed others, suggesting preferential targeting of distinct interneuron types ($n = 41$ PV+ neurons innervated in CA3 and CA1, 36 axons; **Fig. 6b**).

Some axons strongly innervated SATB1−PV+ neurons (putative AACs; $n = 18$ targeted cells in CA3, 17 axons) and bypassed adjacent SATB1+PV+ neurons (**Fig. 6c**). We also followed single septal axons that targeted other CA3 PV+ interneurons but not putative AACs, and in one case observed two SATB1+PV+ neurons each with seven PHA-L boutons apposed to their somata in a 'basket-like' arrangement (**Supplementary Fig. 5a,b**). Similarly to those in CA3, SATB1−PV+ neurons in CA1 were targeted by axons ($n = 6$ cells, 6 axons) that did not innervate nearby SATB1+PV+ neurons (**Supplementary Fig. 5d,e**). We also immunolabeled CA1 pyramidal neurons using the marker SATB2 (ref. 34) but did not observe any septal axons in sPyr innervate these neurons in a basket-like manner around the somata (**Supplementary Fig. 5d**). These data suggest a medial septal input preferentially targeting AACs in both CA3 and CA1.

One population of GABAergic septo-hippocampal axons are immunoreactive for parvalbumin in rat[35]. We tested the axons targeting the SATB1−PV+ neurons for parvalbumin and VGAT[36] using confocal microscopy. Two out of ten axons targeting SATB1−PV+ somata were immunoreactive for parvalbumin, in seven axons parvalbumin was undetectable and in one axon we could not test immunoreactivity. Of the septal boutons apposed to SATB1−PV+ somata, 25.0% were PV+ and in 57.7% parvalbumin was undetectable (17.3% were undetermined; $n = 104$ boutons; 10.4 ± 6.0 per soma observed in fluorescence; mean ± s.d.; **Fig. 6c**). Notably, five of ten axons targeting SATB1+PV+ neurons showed immunoreactivity for parvalbumin (undetectable in two, undetermined in three; **Supplementary Fig. 5c**). Most (72.9% of) septal boutons on SATB1+PV+ somata were PV+ (undetectable in 10.4% and undetermined in 16.6%; $n = 48$ boutons; 4.8 ± 3.2 per soma; **Supplementary Fig. 5c**). Therefore, compared to other PV+ interneurons using immunofluorescence, putative AACs (SATB1−PV+

Figure 5 AACs are SATB1-immunonegative, PV$^+$ interneurons. (**a**) SATB1 (cyan, nuclei) and parvalbumin (magenta) immunoreactivity in a single-optical-section montage of CA3; three PV$^+$ somata in sPyr show nuclear SATB1 immunoreactivity (arrows). (**b**) Three CA3 PV$^+$ neurons (left, magenta) show differential immunoreactivity for SATB1 and SOM (middle panels, cyan and white); neurons are SATB1$^+$ (nucleus, dagger) and SOM$^+$, or immunonegative for both (arrow), or immunoreactive only for SATB1 (asterisk). All three neurons show immunoreactivity for the α1 subunit of the GABA$_A$ receptor (right, yellow). (**c**) Three CA1 PV$^+$ neurons (magenta); two of them are SATB1$^+$ (cyan, asterisks), one is SATB1$^-$ (arrow). All lack immunoreactivity for SOM (white) but are immunopositive for GABA$_A$α1 (yellow). In **b,c**, note the weak GABA$_A$α1 immunoreactivity of the SATB1$^-$ cell. (**d**) A cluster of four CA1 PV$^+$SATB1$^+$GABA$_A$α1$^+$SOM$^-$ neurons (asterisks). (**e**) Quantification of rat and mouse PV$^+$ neurons in sPyr of CA3 (top) and CA1 (bottom), mean ± s.e.m., $n = 4$ areas in each species. (**f**) Neurobiotin-labeled, identified PV$^+$ interneurons (green) and SATB1 immunoreactivity (cyan). Two *in vivo*–recorded CA3 AACs, B44a and B62a, are immunonegative for SATB1 (arrows), but nearby unrecorded neurons (daggers) are immunopositive. Two neurobiotin-labeled CA1 PVBCs, TV08k[20] and M01b, are SATB1$^+$ (asterisks). SATB1 in parentheses indicates mouse anti-SATB2 antibody, which recognizes both SATB2 and SATB1 (**Supplementary Table 2**). Confocal *z*-stack maximum intensity projections; number of optical sections (thickness in μm): **b**, 12 (5.4); **c**, 15 (6.75); **d**, 16 (7.2). Scale bars (μm): **a**, 50; **b–d,f**, 10.
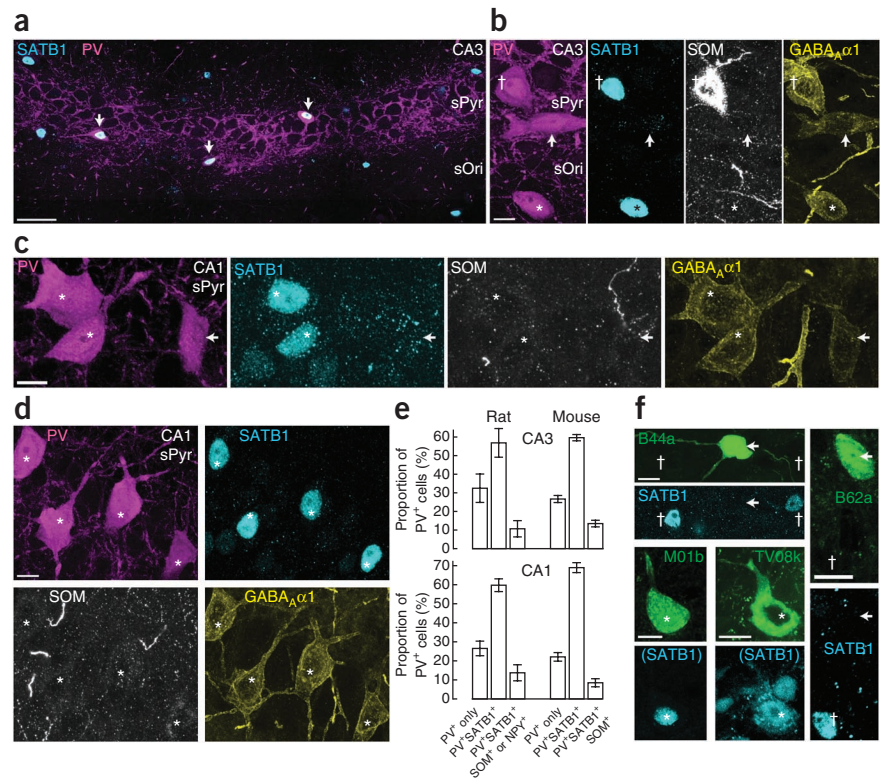
neurons) appeared to be mainly innervated by septal afferents with undetectable levels of parvalbumin. We observed both strongly and weakly parvalbumin-immunoreactive somata in the medial septum (data not shown).

To test the neurotransmitter in soma-innervating septal terminals, we analyzed VGAT-immunoreactivity around PV$^+$ neurons. We observed, for example, a SATB1$^-$ soma but not an adjacent SATB1$^+$ soma innervated by PHA-L$^+$ boutons, which contained VGAT puncta (**Fig. 6d**). GABAergic synapses are rich in the postsynaptic scaffolding protein gephyrin that regulates clustering of GABA$_A$ receptors[37]. Gephyrin-immunoreactive puncta on SATB1$^-$PV$^+$ neurons were aligned with PHA-L$^+$ boutons (**Fig. 6e**). Finally, we asked whether all apposed septal boutons established synapses with the SATB1$^-$PV$^+$ neurons. We identified PHA-L-labeled boutons in apparent contact with putative AAC somata in the light microscope (**Supplementary Fig. 6**). Boutons were electron microscopically sampled from three SATB1$^-$PV$^+$ cells ($n = 15$ of 39 boutons for a cell in CA3, **Supplementary Fig. 6a–e**; $n = 13$ of 29 boutons for another cell in CA3; $n = 11$ of 11 boutons for a cell in CA1), and all were apposed to the plasma membrane of the target cell. Synaptic junctions were found between 11 of 15, 12 of 13 and 10 of 11 boutons and the somata or dendrites (**Supplementary Fig. 6f–j**), some with multiple active zones. In the remaining boutons, the presence of synapses could not be tested owing to an oblique cutting angle. In no case did the boutons innervate any other cells; they made synapses only with the putative AAC. We conclude that all medial septal boutons made synapses with the target AACs, confirming the prediction derived from the gephyrin-immunoreactive puncta (**Fig. 6e**). Therefore, a subpopulation of GABAergic septo-hippocampal axons targets SATB1$^-$PV$^+$ but not SATB1$^+$PV$^+$ somata.

Septo-hippocampal neurons activated during sharp waves

Some medial septal cells increase their firing during hippocampal SWRs but whether they project to the hippocampus is unknown[38,39]. We asked whether any GABAergic septo-hippocampal neurons were activated during sharp waves. We extracellularly recorded and juxtacellularly labeled single medial septal neurons in anesthetized rats (**Fig. 7**). From 31 theta-modulated cells (at $α = 0.05$ with Rayleigh test) that were recorded during >20 SWR events, 12 (38.7%; recorded from 11 rats) showed a variable and significant increase in firing during SWRs (at $α = 0.05$ with Mann Whitney U-tests), on average from $12.0 ± 9.9$ Hz peri-SWR to $28.5 ± 15.6$ Hz (mean ± s.d.; **Fig. 7c,e** and **Supplementary Table 1**). In some cases, the SWR-activated cells fired rhythmically during non-theta periods[40] (not analyzed here), and we also observed activation during events that remained below the threshold for SWR detection with our criteria at the CA1 recording site (**Fig. 7c**). Five of the 12 cells could be labeled and identified, with 5 of 5 and 4 of 4 immunopositive for parvalbumin and hyperpolarization-activated cyclic nucleotide-gated potassium channel 4 (HCN4), respectively (**Fig. 7a**, **Supplementary Fig. 5f,g** and **Supplementary Table 1**). We note that parvalbumin immunoreactivity in the septum does not necessarily imply parvalbumin immunoreactivity in axonal boutons in distant target areas. Notably, 4 of 4 cells were also immunoreactive for SATB1. Of four cells, which were well labeled, two had axons in the fimbria with collaterals entering CA3 (ref. 35) (**Fig. 7b** and **Supplementary Table 1**), but their targets could not be identified. The other two cells had axons in the dorsal fornix and may have projected to the cortex; one of these cells had additional minor branches that entered medial CA1 and subiculum. Septal neurons (3 of 3 tested; **Supplementary Table 1**) were VGAT$^+$ in their local medial septal terminals (**Fig. 7d**) and were thus GABAergic.

Figure 6 A preferential medial septal GABAergic input to the somata of AACs identified by SATB1⁻PV⁺ labeling in CA3. (**a**) PHA-L injection sites in medial septum (cyan, single-optical-section 10× objective montage). Inset, enlargement of boxed region showing three injection sites (circled). Dashed line, midline. (**b**) PHA-L⁺ septo-hippocampal axons (cyan) contact PV⁺ neurons (magenta). The axon (arrows) emits three collaterals; one ends in boutons targeting a PV⁺ soma (box), another targets an unlabeled cell (asterisk). (**c**) Left (from box in **b**), two of three PV⁺ somata (magenta) are SATB1⁺ (white, nuclei); the third is SATB1⁻ and receives septal innervation from the labeled axon (asterisk). Right, two single optical sections (from the z-stack at left) show septal boutons (asterisks) with undetectable immunoreactivity for parvalbumin apposed to the SATB1⁻PV⁺ soma. Axon, arrow. (**d**) Left, one SATB1⁻PV⁺ cell (asterisk) receives PHA-L⁺ innervation (cyan); another SATB1⁺ (cyan nucleus) cell is not innervated. Middle, both somata are surrounded by VGAT⁺ puncta (yellow). Right, single optical

section of the SATB1⁻ cell (asterisk, left image), showing VGAT⁺PHA-L⁺ septal boutons (arrows). (**e**) Top left, dense septal innervation (cyan) of a PV⁺ soma (magenta). Top right, single optical section with additional immunoreactions for SATB1 and NPY (both white), both undetectable in the cell (see **Supplementary Fig. 5d,e**). Bottom, single optical section; PHA-L⁺ boutons on PV⁺ soma colocalize gephyrin puncta (yellow, arrows) but lack detectable parvalbumin immunoreactivity. Confocal z-stacks, number of optical sections (thickness in μm)/intensity projection mode: **b**, 124 (62)/maximum (tile); **c** left, 40 (14)/average; **d**, 50 (16)/average; **e** top left, 68 (21)/average. Scale bars (μm): **a**, both 500; **b**, 20; **c,d**, 10; **e**, 5.
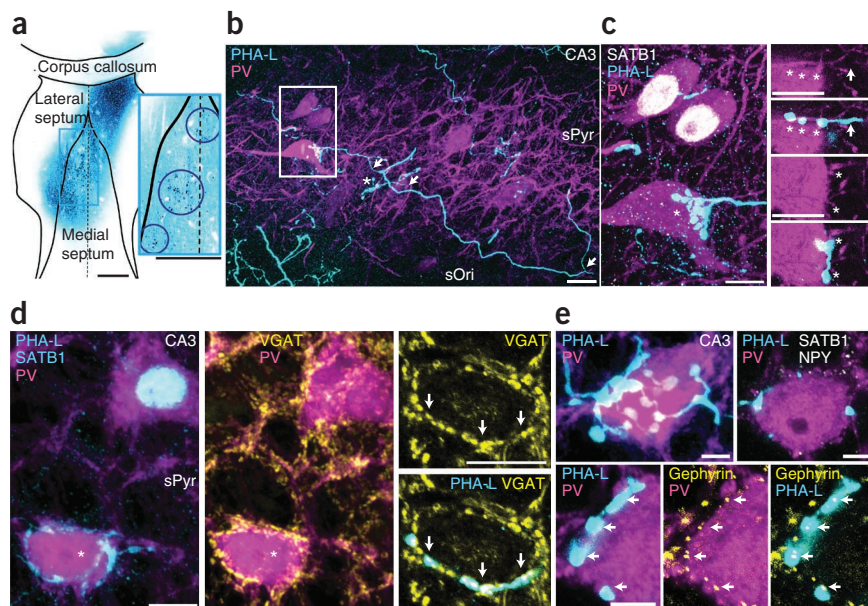
All 12 cells that showed increased firing during SWRs were strongly phase-locked to different phases of theta oscillations (vector lengths of 0.46–0.76; **Supplementary Fig. 5h,i** and **Supplementary Table 1**)[39]. Interestingly, the two CA3-projecting cells fired in a counter-phase manner to the firing of hippocampal AACs (**Fig. 3a**), preferentially at the trough of CA1 theta oscillations (**Supplementary Fig. 5h,i** and **Supplementary Table 1**). We have demonstrated that some septo-hippocampal cells, potentially the sources of AAC innervation, fire in a pattern complementary to AACs during both SWRs and theta oscillations. However, on the basis of differences

in levels of parvalbumin immunoreactivity in PHA-L-labeled septo-hippocampal terminals targeting SATB1⁻PV⁺ somata and the different firing patterns of septal cells, inhibition of AACs may be mediated by more than one medial septal cell type.

DISCUSSION

We have demonstrated that the firing of CA3 AACs is suppressed during sharp waves *in vivo*, resulting in a temporally and spatially restricted reduction of GABA release on the AISs of CA3 pyramidal cells. This is consistent with a key role of AACs in coordinating cell

Figure 7 A subset of GABAergic medial septal cells increase their firing during sharp waves *in vivo* and project to CA3. (**a**) Identified septo-hippocampal GABAergic neuron M82f recorded *in vivo* and shown in a single optical section (soma, neurobiotin, green, left; asterisk). The cell is immunoreactive for parvalbumin (magenta, middle) and HCN4 (cyan, right; arrow, plasma membrane). (**b**) The main axon of M82f in the fimbria of the hippocampus (arrow) branches into CA3 (photographic z reconstruction). (**c**) Some firing patterns of M82f (bottom trace) are associated with the occurrence of SWRs recorded in CA1 (LFP and ripple-filtered LFP in top traces, SWRs plotted in red, arrowheads point to events below the threshold for ripple detection). Note rhythmic firing. (**d**) VGAT-immunoreactive axon boutons (arrows) of M82f in the medial septum (confocal maximum intensity projection z-stack from 7 optical sections, 2.6 μm thick). (**e**) Sharp wave–associated firing rate variation of medial septal cells that fired significantly (at α = 0.05; Mann Whitney U-test) more during SWRs than during peri-SWR periods. Gray area designates the time of SWRs (normalized). Cells are color-coded (left) and those identified with axons projecting to CA3 are shown with thick lines. Scale bars (μm): **a**, 10; **b**, 100; **d**, 5.
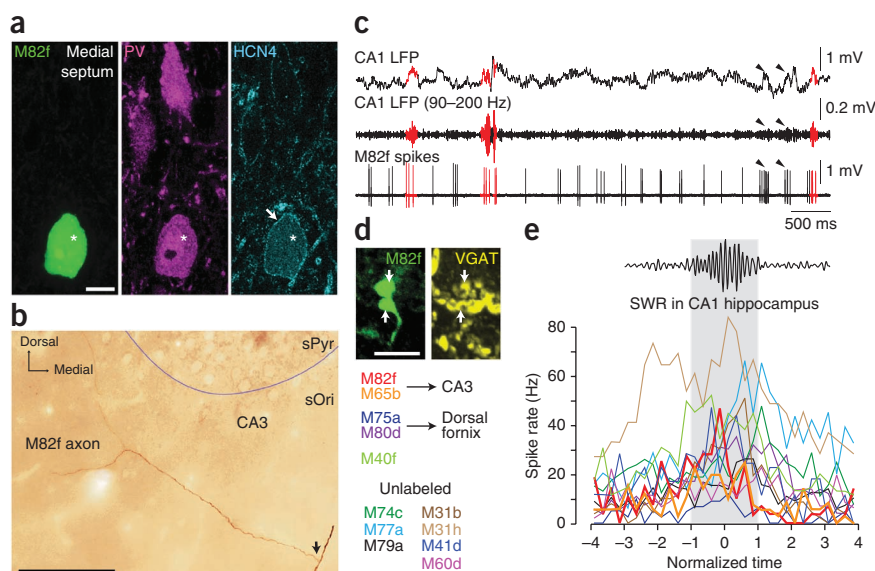
assembly reactivation by allowing excitatory interactions in the CA3 recurrent system selectively during sharp waves[5]. We propose that the inhibition of AACs causes a subcellular redistribution of inhibition from the AIS to the soma and dendrites of pyramidal cells, creating conditions permissive for sharp wave initiation.

We show that the somata of AACs are innervated by a subset of GABAergic medial septal cells that do not target nearby SATB1$^+$PV$^+$ hippocampal neurons and that AACs also receive some dendritic inhibition[14]. Although we recorded SWR-activated septal cells that were immunopositive for parvalbumin, levels of this marker in PHA-L-labeled septal terminals targeting AACs varied. Subsets of septal GABAergic cells[38,39] that project to CA3 fired strongly around the trough of theta oscillations and could innervate AACs. Silencing AACs leads to rhythmic disinhibition of pyramidal cell AISs every 90–200 ms, which could contribute to the theta dipole across hippocampal strata[9,41], resulting in the population of pyramidal cells firing with highest probably at theta trough[23], the minimal firing phase of AACs. These interneurons may also receive recurrent CA3 pyramidal input[42] and entorhinal cortical input to their tufted dendrites in sLacMol, as well as two kinds of mGluR7b-lacking mossy fiber synaptic inputs to dendrites in sLuc, all contributing to their modulation by gamma oscillations.

When the animal becomes quiescent or enters SWS, cholinergic septal input and entorhinal and dentate glutamatergic input change CA3 network excitability in concert with interneurons, and the somatic GABAergic septal input to AACs would possess a different temporal structure than during theta oscillations. Our finding that the suppression of AAC firing during sharp waves occurs irrespective of its local origin at the electrode suggests that a selective and divergent inhibitory input, such as from the septum, silences most AACs. The AACs are synchronized also by means of gap-junction coupling[31]. During the sharp wave, within a 30–120-ms window, AACs may be strongly inhibited by this septal input and probably by other sources of GABA such as local interneurons[14], which may selectively shunt dendritic glutamatergic inputs to AACs. This in turn leads to a withdrawal of GABA from the AIS of pyramidal cells. Disinhibition of the AIS opens a short time window for pyramidal cells to fire at high probability and build up recurrent excitation[43], which enables sharp waves to occur[1] and time-compressed spike sequences to reemerge[44]. Under some *in vitro* conditions, GABA released on the AIS by AACs in the neocortex has been found to be excitatory[45,46]. Our finding that CA3 AACs fire at high frequencies with a temporal pattern inversely related to their postsynaptic targets, confirming previous results in CA1 (ref. 12), suggests that most pyramidal cell spikes are not driven by AACs and most AAC spikes inhibit rather than excite pyramidal cells[46,47], as originally suggested[11].

In contrast to AACs, PVBCs are activated during sharp waves and rhythmically release GABA to the somata and proximal dendrites of pyramidal cells every 4–8 ms. Because CA3 (ref. 24) and CA1 (refs. 12,32) PVBCs are phase locked to local ripple cycles, this cell type, along with strongly activated bistratified cells targeting dendrites[13], may be responsible for generating the fast oscillatory component of SWR events and temporally organizing the pyramidal cell assemblies[5,48].

Both CA3 AACs and PVBCs[24] have access to the same afferents as do pyramidal cells (in contrast to those in CA1; ref. 12), but their strikingly different firing patterns during sharp waves suggests different GABAergic input, matched by their differential expression of SATB1. Indeed, these two cell types have been shown to have divergent network contributions *in vitro*[21]. Future studies in mice may shed light on the functional consequences of altering the relative

GABAergic input specifically to these cell types and on the impact of AACs on sharp-wave initiation. Optogenetic studies exploring the causal relationship between firing of septal cells and AACs would require the establishment of specific markers for septal cell types that target AACs. As SATB1 is expressed by some septo-hippocampal neurons in rats and is also found in the mouse medial septum[30], recording from similar neurons in both wild-type and SATB1 mutant mice[49,50] might provide clues as to how they influence sharp wave generation. To our knowledge, SATB1 represents the first molecular marker that differentiates AACs and PVBCs in the hippocampus, and the septal input represents the first evidence of an identified source of GABAergic input to a single type of hippocampal interneuron. The firing increase of PVBCs and decrease of AACs at the onset of SWRs causes a subcellular redistribution of inhibition in pyramidal cells. According to this concept, AACs, acting as 'gatekeepers', select and control the firing of CA3 pyramidal cell assemblies during the replay of memory sequences.

METHODS

Methods and any associated references are available in the online version of the paper.

Note: Any Supplementary Information and Source Data files are available in the online version of the paper.

AUTHOR CONTRIBUTIONS

T.J.V., B.L., L.K., M.G.C., J.J.T., T.K. and P.S. collected and analyzed data and wrote the paper. To expand on the equal-contributions footnote, each of the first four authors made important—though different—contributions, and hence they should be considered equal first authors.

COMPETING FINANCIAL INTERESTS

The authors declare no competing financial interests.

Reprints and permissions information is available online at http://www.nature.com/reprints/index.html.

1. Buzsáki, G. Hippocampal sharp waves — their origin and significance. *Brain Res.* **398**, 242–252 (1986).
2. O'Keefe, J. & Nadel, L. *The Hippocampus as a Cognitive Map* (Oxford Univ. Press, 1978).
3. Buzsáki, G., Horvath, Z., Urioste, R., Hetke, J. & Wise, K. High-frequency network oscillation in the hippocampus. *Science* **256**, 1025–1027 (1992).
4. Girardeau, G., Benchenane, K., Wiener, S.I., Buzsáki, G. & Zugaro, M.B. Selective suppression of hippocampal ripples impairs spatial memory. *Nat. Neurosci.* **12**, 1222–1223 (2009).
5. Csicsvari, J., Hirase, H., Mamiya, A. & Buzsáki, G. Ensemble patterns of hippocampal CA3–CA1 neurons during sharp wave-associated population events. *Neuron* **28**, 585–594 (2000).
6. Csicsvari, J., Hirase, H., Czurko, A., Mamiya, A. & Buzsáki, G. Oscillatory coupling of hippocampal pyramidal cells and interneurons in the behaving rat. *J. Neurosci.* **19**, 274–287 (1999).
7. Somogyi, P. Hippocampus: intrinsic organization. in *Handbook of Brain Microcircuits* (eds. Shepherd, G.M. & Grillner, S.) 148–164 (Oxford Univ. Press, 2010).
8. Freund, T.F. & Antal, M. GABA-containing neurons in the septum control inhibitory interneurons in the hippocampus. *Nature* **336**, 170–173 (1988).
9. Mizuseki, K., Sirota, A., Pastalkova, E. & Buzsáki, G. Theta oscillations provide temporal windows for local circuit computation in the entorhinal-hippocampal loop. *Neuron* **64**, 267–280 (2009).

10. Szentágothai, J. & Arbib, M.A. Conceptual models of neural organization. *Neurosci. Res. Program Bull.* **12**, 305–510 (1974).
11. Somogyi, P. A specific 'axo-axonal' interneuron in the visual cortex of the rat. *Brain Res.* **136**, 345–350 (1977).
12. Klausberger, T. *et al*. Brain-state- and cell-type-specific firing of hippocampal interneurons *in vivo*. *Nature* **421**, 844–848 (2003).
13. Klausberger, T. *et al*. Spike timing of dendrite-targeting bistratified cells during hippocampal network oscillations *in vivo*. *Nat. Neurosci.* **7**, 41–47 (2004).
14. Gulyás, A.I., Miles, R., Hajos, N. & Freund, T.F. Precision and variability in postsynaptic target selection of inhibitory cells in the hippocampal CA3 region. *Eur. J. Neurosci.* **5**, 1729–1751 (1993).
15. Ishizuka, N., Cowan, W.M. & Amaral, D.G. A quantitative analysis of the dendritic organization of pyramidal cells in the rat hippocampus. *J. Comp. Neurol.* **362**, 17–45 (1995).
16. Fisahn, A., Neddens, J., Yan, L. & Buonanno, A. Neuregulin-1 modulates hippocampal gamma oscillations: implications for schizophrenia. *Cereb. Cortex* **19**, 612–618 (2009).
17. Sugita, S., Ho, A. & Sudhof, T.C. NECABs: a family of neuronal Ca^{2+}-binding proteins with an unusual domain structure and a restricted expression pattern. *Neuroscience* **112**, 51–63 (2002).
18. Jenkins, S.M. & Bennett, V. Ankyrin-G coordinates assembly of the spectrin-based membrane skeleton, voltage-gated sodium channels, and L1 CAMs at Purkinje neuron initial segments. *J. Cell Biol.* **155**, 739–746 (2001).
19. Kosaka, T. The axon initial segment as a synaptic site—ultrastructure and synaptology of the initial segment of the pyramidal cell in the rat hippocampus (CA3 region). *J. Neurocytol.* **9**, 861–882 (1980).
20. Lapray, D. *et al*. Behavior-dependent specialization of identified hippocampal interneurons. *Nat. Neurosci.* **15**, 1265–1271 (2012).
21. Dugladze, T., Schmitz, D., Whittington, M.A., Vida, I. & Gloveli, T. Segregation of axonal and somatic activity during fast network oscillations. *Science* **336**, 1458–1461 (2012).
22. Tukker, J.J., Fuentealba, P., Hartwich, K., Somogyi, P. & Klausberger, T. Cell type-specific tuning of hippocampal interneuron firing during gamma oscillations *in vivo*. *J. Neurosci.* **27**, 8184–8189 (2007).
23. Lasztóczi, B., Tukker, J.J., Somogyi, P. & Klausberger, T. Terminal field and firing selectivity of cholecystokinin-expressing interneurons in the hippocampal CA3 area. *J. Neurosci.* **31**, 18073–18093 (2011).
24. Tukker, J.J. *et al*. Distinct dendritic arborization and *in vivo* firing patterns of parvalbumin-expressing basket cells in the hippocampal area CA3. *J. Neurosci.* **33**, 6809–6825 (2013).
25. Richter, K. *et al*. Presynaptic cytomatrix protein Bassoon is localized at both excitatory and inhibitory synapses of rat brain. *J. Comp. Neurol.* **408**, 437–448 (1999).
26. Dávid, C., Schleicher, A., Zuschratter, W. & Staiger, J.F. The innervation of parvalbumin-containing interneurons by VIP-immunopositive interneurons in the primary somatosensory cortex of the adult rat. *Eur. J. Neurosci.* **25**, 2329–2340 (2007).
27. Acsády, L., Kamondi, A., Sik, A., Freund, T. & Buzsáki, G. GABAergic cells are the major postsynaptic targets of mossy fibers in the rat hippocampus. *J. Neurosci.* **18**, 3386–3403 (1998).
28. Shigemoto, R. *et al*. Differential presynaptic localization of metabotropic glutamate receptor subtypes in the rat hippocampus. *J. Neurosci.* **17**, 7503–7522 (1997).
29. Szabadics, J., Varga, C., Brunner, J., Chen, K. & Soltesz, I. Granule cells in the CA3 area. *J. Neurosci.* **30**, 8296–8307 (2010).
30. Huang, Y. *et al*. Distribution of Satb1 in the central nervous system of adult mice. *Neurosci. Res.* **71**, 12–21 (2011).
31. Baude, A., Bleasdale, C., Dalezios, Y., Somogyi, P. & Klausberger, T. Immunoreactivity for the $GABA_A$ receptor alpha1 subunit, somatostatin and Connexin36 distinguishes axoaxonic, basket, and bistratified interneurons of the rat hippocampus. *Cereb. Cortex* **17**, 2094–2107 (2007).
32. Varga, C., Golshani, P. & Soltesz, I. Frequency-invariant temporal ordering of interneuronal discharges during hippocampal oscillations in awake mice. *Proc. Natl. Acad. Sci. USA* **109**, E2726–E2734 (2012).
33. Swanson, L.W. & Cowan, W.M. The connections of the septal region in the rat. *J. Comp. Neurol.* **186**, 621–655 (1979).
34. Nielsen, J.V., Blom, J.B., Noraberg, J. & Jensen, N.A. Zbtb20-induced CA1 pyramidal neuron development and area enlargement in the cerebral midline cortex of mice. *Cereb. Cortex* **20**, 1904–1914 (2010).
35. Freund, T.F. GABAergic septohippocampal neurons contain parvalbumin. *Brain Res.* **478**, 375–381 (1989).
36. Chaudhry, F.A. *et al*. The vesicular GABA transporter, VGAT, localizes to synaptic vesicles in sets of glycinergic as well as GABAergic neurons. *J. Neurosci.* **18**, 9733–9750 (1998).
37. Fritschy, J.-M., Harvey, R.J. & Schwarz, G. Gephyrin: where do we stand, where do we go? *Trends Neurosci.* **31**, 257–264 (2008).
38. Varga, V. *et al*. The presence of pacemaker HCN channels identifies theta rhythmic GABAergic neurons in the medial septum. *J. Physiol.* (*Lond.*) **586**, 3893–3915 (2008).
39. Borhegyi, Z., Varga, V., Szilagyi, N., Fabo, D. & Freund, T.F. Phase segregation of medial septal GABAergic neurons during hippocampal theta activity. *J. Neurosci.* **24**, 8470–8479 (2004).
40. Dragoi, G., Carpi, D., Recce, M., Csicsvari, J. & Buzsáki, G. Interactions between hippocampus and medial septum during sharp waves and theta oscillation in the behaving rat. *J. Neurosci.* **19**, 6191–6199 (1999).
41. Zhang, L. *et al*. Hippocampal theta-driving cells revealed by Granger causality. *Hippocampus* **22**, 1781–1793 (2012).
42. Papp, O.I., Karlócai, M.R., Tóth, I.E., Freund, T.F. & Hájos, N. Different input and output properties characterize parvalbumin-positive basket and axo-axonic cells in the hippocampal CA3 subfield. *Hippocampus* **23**, 903–918 (2013).
43. Miles, R. Synaptic excitation of inhibitory cells by single CA3 hippocampal pyramidal cells of the guinea-pig in vitro. *J. Physiol.* (*Lond.*) **428**, 61–77 (1990).
44. Wilson, M.A. & McNaughton, B.L. Reactivation of hippocampal ensemble memories during sleep. *Science* **265**, 676–679 (1994).
45. Szabadics, J. *et al*. Excitatory effect of GABAergic axo-axonic cells in cortical microcircuits. *Science* **311**, 233–235 (2006).
46. Woodruff, A.R. *et al*. State-dependent function of neocortical chandelier cells. *J. Neurosci.* **31**, 17872–17886 (2011).
47. Glickfeld, L., Roberts, J., Somogyi, P. & Scanziani, M. Interneurons hyperpolarize pyramidal cells along their entire somatodendritic axis. *Nat. Neurosci.* **12**, 21–23 (2009).
48. Gulyás, A.I. *et al*. Parvalbumin-containing fast-spiking basket cells generate the field potential oscillations induced by cholinergic receptor activation in the hippocampus. *J. Neurosci.* **30**, 15134–15145 (2010).
49. Denaxa, M. *et al*. Maturation-promoting activity of SATB1 in MGE-derived cortical interneurons. *Cell Rep.* **2**, 1351–1362 (2012).
50. Close, J. *et al*. Satb1 is an activity-modulated transcription factor required for the terminal differentiation and connectivity of medial ganglionic eminence-derived cortical interneurons. *J. Neurosci.* **32**, 17690–17705 (2012).

ONLINE METHODS

***In vivo* recording, labeling, electrophysiological and statistical analyses.** All procedures involving experimental animals were under approved personal and project licenses in accordance with the Animals (Scientific Procedures) Act, 1986 (UK) and associated regulations. Methods have been described in detail elsewhere[23]. Briefly, 250–350-g adult male Sprague-Dawley rats (housed with littermates on a normal light-dark cycle, lights on 08:00 to 20:00, 19–21 °C, 55% humidity) were anesthetized by urethane (1.25 g kg^{-1}, intraperitoneally), with supplemental doses of ketamine and xylazine (20 and 2 mg kg^{-1}, intraperitoneally; except for rat B62, which was given 5 and 2 mg kg^{-1}) as necessary. LFPs (0.3–300 Hz; 1 kHz sampling) were recorded by a glass electrode aimed at CA1 sPyr (4 mm posterior and 2 mm right from bregma, 10° postero-anterior angle, ~2.3 mm deep). LFPs and action potentials (0.8–5 kHz; 20 kHz sampling) of individual neurons were recorded by a glass electrode in CA3 (2.8 mm posterior and 2.8–3.8 mm right from bregma, 10° antero-posterior angle) or medial septum (0.6 mm anterior and 1.4 mm left from bregma, 15° latero-medial angle). The recorded cell was subsequently juxtacellularly labeled[51] with 1.5% neurobiotin (3% for medial septal cells) in 0.5 M NaCl. A recovery time of 4–10 h was used for medial septal cells. In some experiments, additional recordings were made by a tetrode pair inserted into CA3 sPyr[23]. For experiments in freely moving rats, methods have been previously described[20]. Adult rats LK24 and TV34 weighed 450 g and 477 g, respectively, at the time of headstage implantation. They were housed on a reverse light-dark cycle with the same temperature and humidity as described above. Buprenorphine (Vetergesic, 0.03 mg kg^{-1}, subcutaneously) was used peri-operatively for headstage implantation and craniotomy and duratomy procedures. Recordings began at least 24 h after the craniotomy over CA1–CA3, and a 3% neurobiotin solution in 0.5 M NaCl was used for juxtacellular labeling.

Analyses were performed in Spike2 (CED, Cambridge, UK) and MATLAB. We identified SWRs in anesthetized rats on the basis of the 90–200 Hz root-mean-square amplitude exceeding a threshold (5 s.d.; except J54a, for which the CA1 electrode was in sRad and we used 4 s.d. to improve detection). We detected SWRs in CA1 (6 experiments) or, when possible, in CA3 (3 experiments; CA3 glass electrode in B62 and J67, and one of the tetrode wires in B45). In freely moving rats, we used 130–230 Hz filtering[20], 4 s.d. threshold from the glass electrode. Theta and non-theta periods were identified in anesthetized rats on the basis of a theta (3–6 Hz) to delta (2–3 Hz) power ratio in the CA1 (or CA3 in J67) electrode of >4 (theta) or <2 (non-theta; SWRs were excluded) for at least 6 s. In freely moving rats, we used a 5–12 Hz theta to 2–4 Hz delta ratio[20]. The identified periods were taken as samples and firing rate comparisons were made by the Mann-Whitney *U*-test.

Theta phase was calculated by linear interpolation between troughs (designated 0° and 360°) identified in 3–6 Hz band-pass filtered traces for anesthetized experiments. For uniformity of circular phase distributions, we used the Rayleigh test[23], taking the mean phase and mean vector length as descriptive statistics for phase preference and coupling strength, respectively. Cell J54a was excluded from mean CA1 theta phase calculations because the CA1 electrode was in sRad instead of sPyr. Cell B53b was excluded from mean firing rate calculations because of unusually deep anesthesia.

To identify effects of SWRs on firing rates, the distribution of the numbers of action potentials during SWRs were compared to the distribution in identical time windows randomly placed 100 times in the ±10-s vicinity of the SWR (with other SWRs excluded; peri-SWR data)[23]. Distributions were compared by a Mann-Whitney *U*-test. We also analyzed temporal dynamics of firing during SWRs and created rate histograms as a function of normalized time, as previously described[12,23], averaged across different cells and statistically assessed with a one-way ANOVA. Individual bins were considered significant when a *post hoc* Tukey test disclosed a significant difference to at least one of the baseline bins (the first 12 bins of the histogram). The recording of B53b only had 7 SWRs so was not included in further statistical analyses, but its firing was qualitatively consistent with the other AACs.

Coupling to gamma oscillations was analyzed by calculating circular means of spike phase spectra (15–100 Hz; extracted with wavelet transformation), as previously described[23]. Spectra for all spikes but those during SWRs were included. For the local (CA3) glass electrode LFP, "spike artifacts" were substituted by linearly interpolated values.

No statistical methods were used to predetermine sample sizes but our sample sizes are similar to those reported in previous publications[12,20,23]. For some

statistical tests used in this study data distribution was assumed to be normal (or von Mieses for circular data) but this was not formally tested.

Anterograde tracing. A 2.5% w/v solution of PHA-L (L-1110, Vector Laboratories)[52] in 0.1 M phosphate buffer (PB) was injected into the medial septum of 3 rats under isoflurane anesthesia. Coordinates from bregma: 0.6 mm anterior, 1.4 mm left, with a 15° latero-medial angle. Iontophoresis was used to deliver PHA-L (5 μA positive current, 7 s duty cycle, 10–30 min delivery times) at 3 slightly different locations (6.5, 5.8, 5.5 mm depth from the brain surface for one rat; 6.2, 5.8, 5.5 mm for the other two rats). The electrode was placed at the first location for 15 min before stimulation and not moved until 5 min after each injection. Electrode tip diameter was ~10 μm. Following recovery, animals were kept for 4–18 days until perfusion. To assess the spatial extent of PHA-L delivery from within the septum, a fourth rat was injected in the lateral septum (6.2, 5.8, 5.5 mm depth, 10 min delivery times).

Tissue processing. After transcardial perfusion (4% paraformaldehyde, 15% v/v saturated picric acid and 0.05% glutaraldehyde in 0.1 M PB), brains were stored in 0.1 M PB with 0.05% sodium azide (PB-Az) at 4 °C. Coronal sections (70 μm; Leica VT 1000S vibratome) were washed three times in 0.1 M PB and stored in PB-Az at 4 °C. To find neurobiotin-labeled neurons, sections were either permeabilized in Tris-buffered saline (TBS) with 0.1% Triton X-100 (Tx) or subjected to one or two rounds of freeze-thaw over liquid nitrogen after cryoprotecting in 20% sucrose. After three or four washes in 0.1 M PB, sections were incubated in 1:1,000 streptavidin-conjugated Alexa Fluor 488 (Invitrogen) in TBS or TBS-Tx for 4 h at room temperature (RT) or overnight at 4 °C. After three washes, sections were mounted on slides in VectaShield (Vector Laboratories). For analysis, electron microscopy and reconstruction, sections were processed with the horseradish peroxidase (HRP) reaction to reveal neurobiotin with a diaminobenzidine (DAB) reaction product. Sections were incubated in 1:100 avidin–biotinylated peroxidase complex (ABC; Vectastain ABC Elite kit, Vector Laboratories) in TBS-Tx or TBS for 2–3 d at 4 °C. If sections were previously incubated in streptavidin, sections were additionally incubated with the biotinylated peroxidase complex for 4 h at RT or overnight at 4 °C before incubating in ABC. After three washes in 0.1 M PB, sections were incubated in a 0.5 mg/ml DAB (Sigma-Aldrich) solution containing glucose, ammonium chloride and 0–4% nickel ammonium sulfate. After 15 min, 0.2% glucose oxidase was added to generate H_2O_2 for the oxidation of DAB by peroxidase, forming a blue-black precipitate in the presence of nickel. After 40–60 min, depending on the darkness of the reaction product, sections were washed four times in 0.1 M PB. Next, sections were incubated in 0.2–1% osmium tetroxide in 0.1 M PB for 1 h and washed three times in 0.1 M PB. Sections were dehydrated in successive rounds of ethanol (50%, 70%, 90%, 95%, 100%), followed by propylene oxide (VWR International). Between the 70% and 90% ethanol washes, sections were incubated for 40 min in 2% uranyl acetate in 70% ethanol to enhance contrast for electron microscopy (see below). Next, sections were submerged in epoxy resin (Durcupan ACM Fluka, Sigma-Aldrich) and left overnight. Finally, sections were mounted on slides under a coverslip and the resin was polymerized at 60 °C for >24 h.

Immunohistochemistry. For sections subjected to freeze-thaw, TBS was used for all base solutions and washes. Otherwise, TBS-Tx was used throughout. Sections were blocked for 1 h in 10% normal horse serum (NHS) before application of a primary antibody solution containing 1% NHS for 3 d at 4 °C. Negative controls lacked the primary antibodies. See **Supplementary Table 2** for specificity information and dilutions. After incubation, sections were washed three times for 10 min each and then incubated in secondary antibody solution containing 1% NHS. The following secondary antibodies were used: donkey anti-rabbit Alexa Fluor 405 (1:250, Invitrogen; A31556 lot 55310A); donkey anti-mouse, anti-goat or anti–guinea pig DyLight405 (1:250, Jackson ImmunoResearch Laboratories; 715-475-151 lot 98883, 705-475-147 lot 96706, 706-475-148 lot 99779, respectively); donkey anti-rabbit or anti-goat Alexa Fluor 488 (1:1,000, Invitrogen; A21206 lot 556439, A11055 lot 49732A, respectively); donkey anti-rabbit, anti-goat, anti-sheep, anti-mouse or anti–guinea pig Cy3 (1:400, Jackson; 711-165-152 lot 98888, 705-165-147 lot 81185, 713-165-147 lot 87933, 715-165-151 lot 94510, 706-165-148 lot 86928, respectively); donkey anti-rabbit, anti-goat, anti-sheep, anti-mouse or anti–guinea pig Cy5 (1:250, Jackson; 711-175-152 lot 80443, 705-175-147 lot 72031, 713-175-147

lot 72156, 715-175-151 lot 88814, 706-175-148 lot 72155, respectively); donkey anti-rabbit, anti-goat or anti-mouse DyLight 649 (1:250, Jackson; 711-495-152 lot 98016, 705-495-147 lot 97534, 715-495-151 lot 94507, respectively), donkey anti-sheep or anti–guinea pig Alexa Fluor 647 (1:250, Jackson; 713-605-147 lot 102770, 706-605-148 lot 100905, respectively); donkey anti–guinea pig HRP (1:100, Jackson); and swine anti-rabbit HRP (1:100, Dako, Glostrup, Denmark; P0217). After 4 h at room temperature or 4 °C overnight, sections for immuno-fluorescence were washed three times for 10 min each and mounted on glass slides in VectaShield. For two-color DAB-based HRP enzyme reactions (rabbit anti-VGAT and neurobiotin), freeze-thawed sections were incubated in primary antibody as above, processed with ABC and then processed with DAB (without Ni^{2+}) and glucose oxidase to react the neurobiotin-labeled cell. Next sections were washed four times in 0.1 M PB and incubated overnight in anti-rabbit HRP secondary antibody solution. Sections were processed for DAB but using H_2O_2 as the substrate directly for 2–7 min. Processing continued as above. In experiments that used the biotinylated anti–PHA-L primary antibody, streptavidin Alexa Fluor 488 was used for fluorescence visualization followed by conversion with DAB as above (4% nickel ammonium sulfate).

Confocal imaging. An LSM710 confocal microscope (Axio Imager.Z1, Carl Zeiss) with ZEN 2008 software v5.0 (Zeiss) was used to acquire multi-channel fluorescence images. DIC M27 Plan-Apochromat 63×/1.4 n.a. and alpha Plan-Apochromat 100×/1.46 n.a. oil immersion objectives were used with the following channels (laser and excitation wavelength, fluorophores, beam splitters, emission spectral filter): 405-30 solid state 405 nm with attenuation filter ND04, DyLight405, MBS-405, 409–499 nm; argon 488 nm, Alexa Fluor 488, MBS-488, 493–542 nm; HeNe 543 nm, Cy3, MBS-458/543, 552–639 nm; HeNe 633 nm, Cy5/DyLight 649/Alexa Fluor 647, MBS 488/543/633, 637–757 nm. Channels were acquired sequentially with an eight-bit dynamic range, and the pinhole size was set at 1 Airy unit for the shortest wavelength used; the pin-hole sizes of the other channels were adjusted to values <1 Airy unit, giving all channels the same optical slice thickness. With the 63× lens and the 405-30 laser, the optical slice thickness was typically 0.6 μm. Using the argon laser as the shortest excitation wavelength, 1 Airy unit gave an optical slice thickness of 0.7 μm. Pixel number was calculated with Nyquist sampling, optimized for the channel having the shortest wavelength. At 63× with the 405-30 laser, sampling resolution was typically 12.686 pixel $μm^{-1}$, $0.08 × 0.08 × 0.43$ μm voxels. At 100×, sampling was 13.173 pixel $μm^{-1}$. We used the 63× lens for the majority of 3D images due to higher transmission, including for montages (zoomed out by 0.8). Assignment of antibody fluorophores was based on minimizing spectral overlap between channels. Synaptic markers were assigned the highest resolution channel. In some cases where markers showed no spatial overlap, two markers were sometimes labeled with the same fluorophore, increasing the number of markers used within one section: for example, gephyrin DyLight405 (post-synaptic puncta); SATB2 and PHA-L AF488 (nuclei and axons); SATB1 and NPY Cy3 (nuclei and Golgi apparatus); and parvalbumin DyLight649 (cytoplasm). Images were analyzed in ImageJ. Deconvolution (ZEN 2008) was used before quantifying bassoon puncta.

Quantification of immunolabeled neurons. To quantify SATB1 immuno-activity in PV+ neurons, cells in dorsal CA1 and CA3 of 70-μm-thick sections (from both adult rats and C57/BL6 mice) were counted using widefield epi-fluorescence on a Leitz DMRB microscope (Leica) equipped with PL Fluotar objectives. We counted only cells that had whole somata within sPyr, with the condition that the nucleolus must be visible in the fluorescence channel corresponding to parvalbumin. Cells were marked SATB1-immunonegative only when the mean pixel intensity of the nuclear region was the same as a background region of interest in the SATB1 channel. To confirm immuno-positivity or immunonegativity, counted cells were sometimes scanned with the confocal microscope.

To quantify parvalbumin immunoreactivity in PHA-L-labeled septal axon terminals in the hippocampus, confocal microscopic z-stacks were analyzed. As a positive control, reference PHA-L-labeled axons immunopositive for par-valbumin were located at different depths in the z-stack of each brain section. Axons deep in the stack were excluded because of the lower signal-to-noise ratio. "Immunopositive" was defined as positive pixels in the axon or in axon boutons, similar to those in the positive control, compared to the background.

"Undetectable" defines the limit of our method; we cannot rule out low parvalbumin immunoreactivity. "Undetermined" corresponds to PHA-L-labeled axons or axon boutons that were obscured by the parvalbumin immunoreactivity of larger structures.

Electron microscopy. Target areas (for example, axon-rich regions, or dendrites in sLuc) were cut from the resin-embedded 70-μm-thick sections and reem-bedded for ultramicrotome sectioning. Serial electron microscopic sections were cut and mounted on single-slot, pioloform-coated copper grids. A Philips CM100 transmission electron microscope fitted with a Gatan UltraScan 1000 CCD camera was used to acquire images. All boutons cut by the section plane were followed in serial sections and searched for synaptic junctions. AISs were identified as previously described[11]. All synapses found innervated AISs; none of the boutons could be shown to make a synapse with a dendrite or a soma. As the AISs are relatively small in diameter and may have tortuous courses, the membrane of boutons and the apposed AIS membrane is cut at an oblique angle in many cases, which makes it impossible to reveal the synaptic cleft even with tilting the sections in the electron microscope. Such cases were not counted. Initial identification of axon cartridges[14] at the light microscopic level (and their association with AISs using ankyrin G immunoreactivity) correlated with the electron microscopic results. Mossy fibers were scanned in the vicinity of AAC dendrites in sLuc. Only clearly identified synapses were quantified. Nonlinear contrast adjustment was applied to all images.

Digital reconstruction and quantification. The full dendritic trees of three AACs were reconstructed in 3D from the series of nominally 70-μm-thick coro-nal sections. Dendrites were traced using Neurolucida (v.9, MBF Bioscience) on a Nikon Eclipse 80i microscope equipped with a Lucivid and a 100× 1.4 n.a. oil immersion Plan Apo VC objective lens. Laminar boundaries were drawn for all sections in Neurolucida and crossing points for all dendrites were checked indi-vidually and recorded. The outline of each section was also traced as a general reference for rotational alignment and confirmation of shrinkage correction. To aid the delineation of laminar and areal boundaries, immunoreactivity to mGluR2/3 (for sRad–sLacMol and sLuc–sRad)[28] and calbindin (for sLuc–sRad and CA3–CA2)[53] was sometimes tested on the sections with immunofluores-cence and in immunoperoxidase reactions.

Because of tissue shrinkage, each section was expanded to its original unpro-cessed dimensions by applying shrinkage correction ratios, whenever possible using individual section values. In order to compensate for z-axis shrinkage, the section thickness was measured by visualizing the top and bottom surfaces of the tissue using DAPI staining, a Colibri 405-nm LED and the Axio Imager. Z1 microscope with the 100× 1.46 n.a. oil immersion objective lens. The mean thickness was calculated for each section from at least five z measurements taken along CA1, CA3 and dentate gyrus. Postprocessing (epoxy resin–embedded) section thickness was measured in Neurolucida. In some cases, the correction was done using the mean preprocessing thickness calculated from nondendritic sections. The same methods were applied for the lateral dimensions from images taken before and after processing.

Dendrites of B45a, B10a, J54a spanned 11, 11 and 9 consecutive sections, respectively. For B45a, freeze-thawed and Triton-treated dendritic sections had mean z dimension shrinkage correction ratios of $1.31 ± 0.07$ (s.d.) and $1.40 ± 0.1$, respectively. For x-y dimensions, the mean ratio for the freeze-thawed den-dritic sections was $1.06 ± 0.02$; dimensions of Triton-treated dendritic sections were scaled manually in Neurolucida to match the other corrected sections. For B10a, the mean shrinkage correction ratios were $1.07 ± 0.17$ (freeze-thawed dendritic sections) and $1.27 ± 0.15$ (Triton-treated dendritic sections) for the z dimension. For x-y dimensions, mean ratios were $1.05 ± 0.02$ (freeze-thawed) and $1.08 ± 0.01$ (Triton-treated); four dendritic sections were scaled manually. For J54a, the mean shrinkage correction ratios were $1.13 ± 0.11$ (freeze-thawed) and $1.20 ± 0.14$ (Triton-treated) for the z dimension. For x-y dimensions, the mean shrinkage correction ratios were $1.04 ± 0.02$ (freeze-thawed) and $1.12 ± 0.03$ (Triton-treated).

The total dendritic length per stratum in the shrinkage-corrected and spliced reconstructions was calculated using Neurolucida Explorer. For figures, reconstructions were rotated to obtain a semi-coronal projection, providing the maximum overlap between corresponding laminar boundaries from con-secutive sections. A representative part of the B45a axon, initially drawn on

paper with a drawing tube, was photographed and superimposed onto the reconstructed dendrites.

51. Pinault, D. A novel single-cell staining procedure performed *in vivo* under electrophysiological control: morpho-functional features of juxtacellularly labeled thalamic cells and other central neurons with biocytin or neurobiotin. *J. Neurosci. Methods* **65**, 113–136 (1996).

52. Gerfen, C.R. & Sawchenko, P. An anterograde neuroanatomical tracing method that shows the detailed morphology of neurons, their axons and terminals: immunohistochemical localization of an axonally transported plant lectin, *Phaseolus vulgaris* leucoagglutinin (PHA-L). *Brain Res.* **290**, 219–238 (1984).

53. Sloviter, R.S. Calcium-binding protein (calbindin-D28k) and parvalbumin immunocytochemistry: localization in the rat hippocampus with specific reference to the selective vulnerability of hippocampal neurons to seizure activity. *J. Comp. Neurol.* **280**, 183–196 (1989).

Network state-dependent inhibition of identified hippocampal CA3 axo-axonic cells in vivo.

Tim J Viney*, Balint Lasztoczi*, Linda Katona*, Michael G Crump*, John J Tukker, Thomas Klausberger, Peter Somogyi

a

b

c
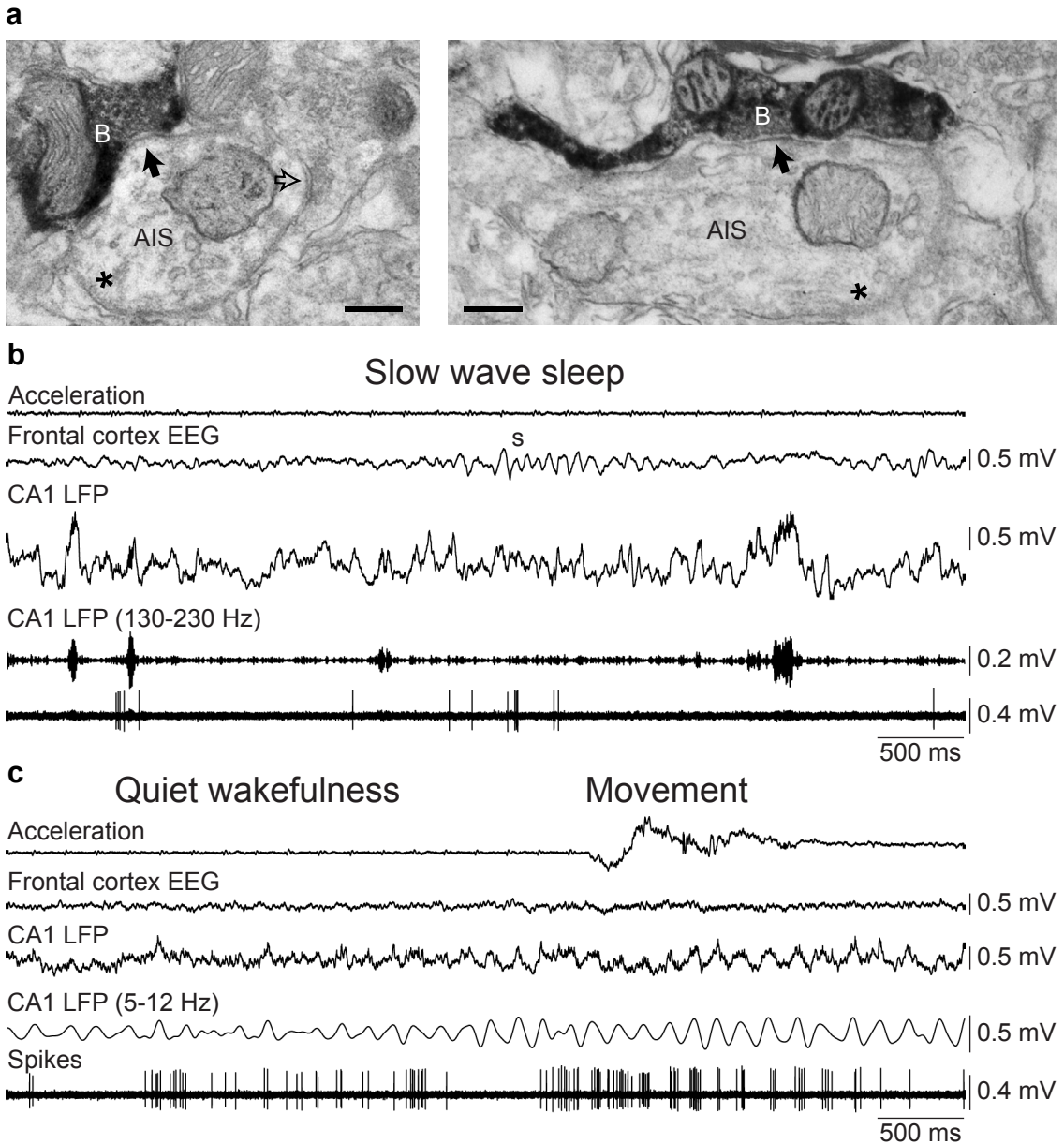
Supplementary Figure 1. A CA1 axo-axonic cell recorded in a freely moving rat is inhibited during sharp waves. (**a**) Left, a bouton (B) of cell TV34n filled with electron opaque HRP reaction end-product making a type II synapse (filled arrow) with a pyramidal cell AIS (identified by the dense membrane undercoating, asterisk); open arrow, a type II synapse with an unlabeled bouton. Right, another bouton of the same cell. Scale bars, 0.2 μm. (**b** and **c**) Firing patterns of the identified AAC TV34n during (**b**) SWS and (**c**) during quiet wakefulness and head movement. Movement is detected by an accelerometer; spindles (s) are present in the EEG during SWS.
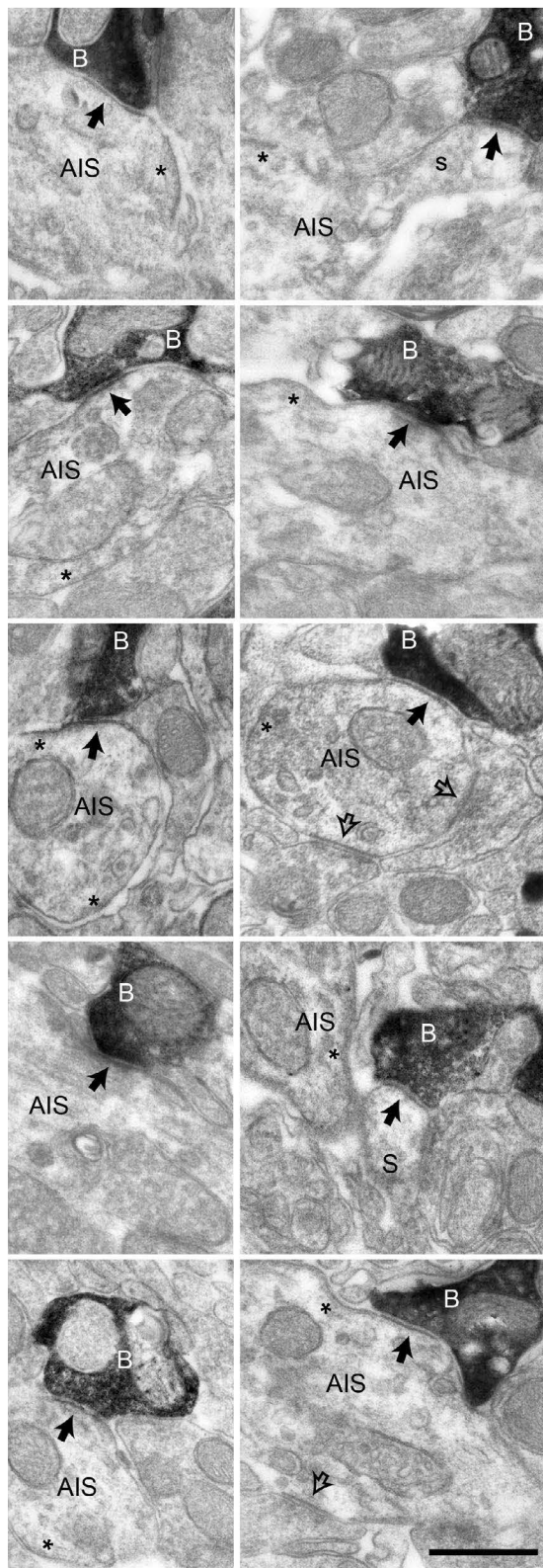
Supplementary Figure 2. Synaptic junctions between the boutons of identified CA3 axo-axonic cells and axon initial segments of pyramidal cells.

Supplementary Figure 2 (continued). Ten electron micrographs taken from serial sections of neurobiotin-labeled (HRP end-product) boutons (B) of AAC B45a making type II synapses (arrows) with AISs, identified by membrane undercoating (asterisks) and/or microtubule fascicles. Unlabeled boutons also make similar synapses (open arrows). Spines (s) from AISs, described previously (ref. 19), also receive one or more AAC synapses. Sections were not contrasted by lead. Scale for all images: 0.5 μm.
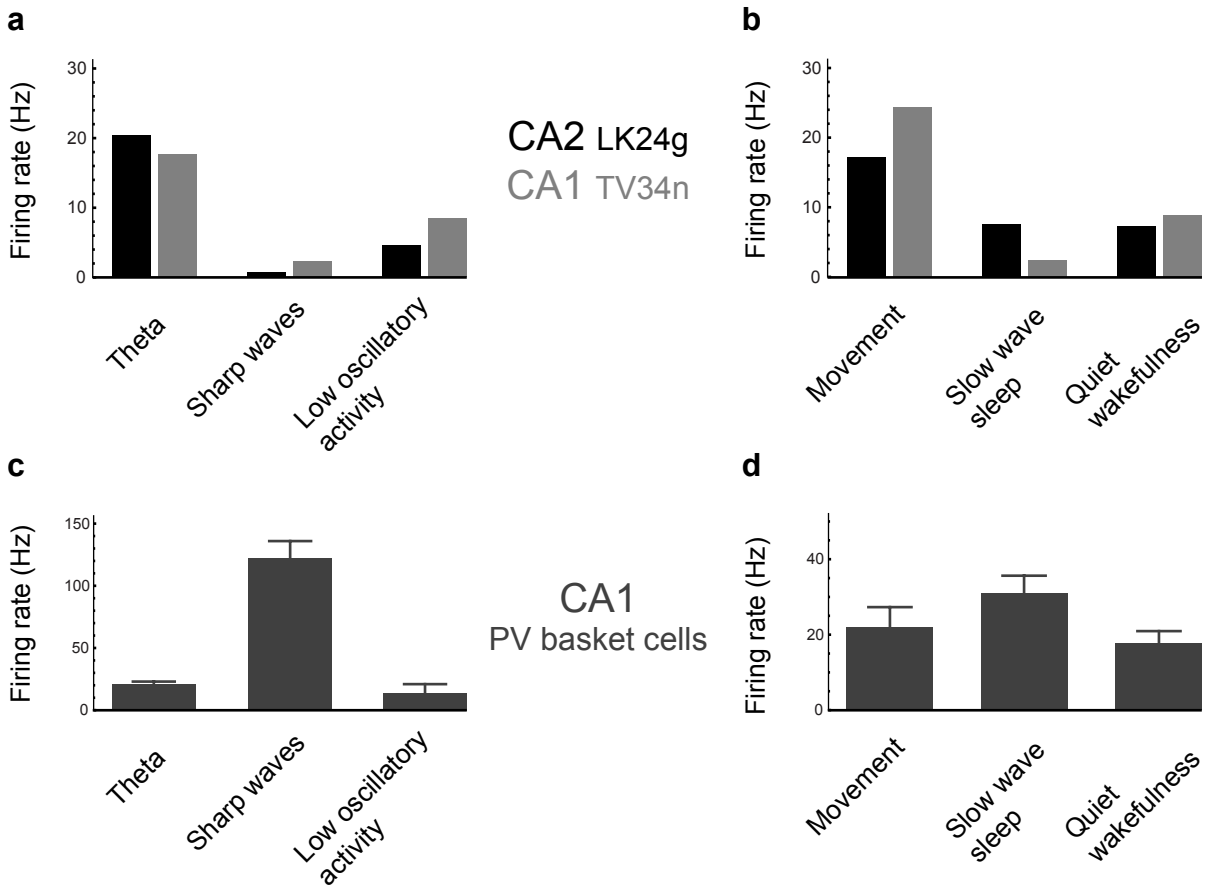
Supplementary Figure 3. State-dependent firing rates of identified axo-axonic cells in freely moving rats. (**a** and **b**) Firing rates of identified CA2 AAC LK24g (black) and CA1 AAC TV34n (gray) during (**a**) network oscillations and (**b**) behavioral states. (**c** and **d**) Mean ± s.e.m. firing rates of 5 published identified parvalbumin-expressing basket cells (ref. 20) for comparison with the AACs. Note the different rates during sharp waves when compared to theta oscillations.
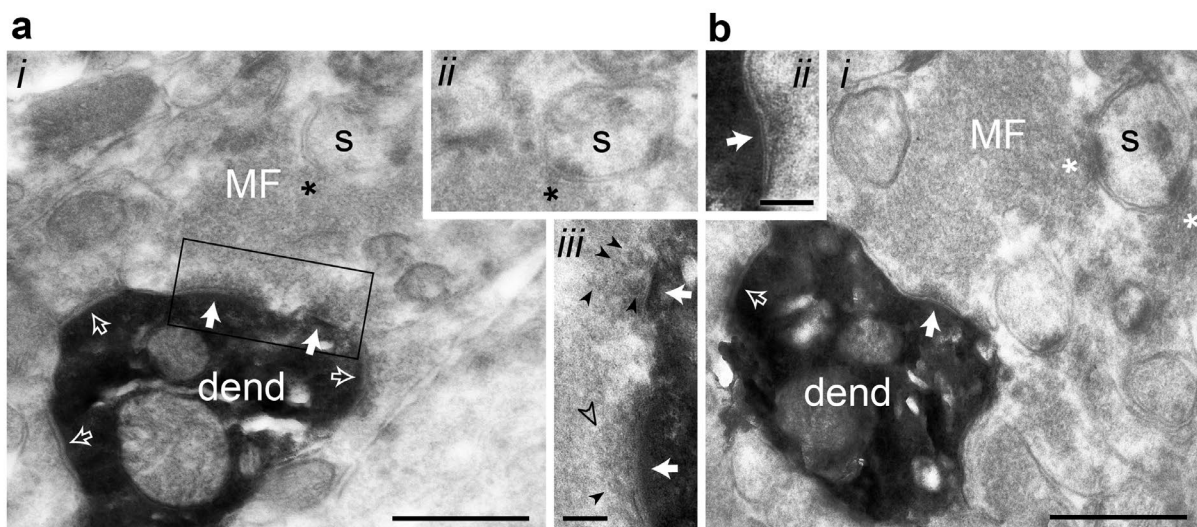
Supplementary Figure 4. Innervation of axo-axonic cell dendrites by mossy fiber terminals. (**a**,**i**) Electron micrograph of a neurobiotin-labeled AAC dendrite in sLuc (dend, cell B45a) receiving synaptic input (filled white arrows) from a large mossy fiber bouton (MF) recognized by dense vesicular filling. Unfilled white arrows, synapses made by boutons other than the large mossy terminal; s, invaginated spine from a thorny excrescence of a CA3 pyramidal cell dendrite. (**a**,**ii**) Serial section of the spine (s) with synaptic junction (asterisk). (**a**,**iii**) Enlargement of synaptic junctions in **i** (white arrows). Image captured at a different angle of tilt. Black arrowheads, synaptic vesicles; open arrowhead, dense core vesicle. (**b**) Same as in **a**,**i**; another large mossy terminal (MF) making a synapse (white arrow, see inset **b**,**ii**) onto the same dendrite. Asterisks, synapses by the mossy terminal on a pyramidal cell spine (s). Sections were not contrasted by lead. Scale bars: **a**,**i**, **a**,**ii**, **b**,**i**, 0.5 µm; **a**,**iii**, **b**,**ii**, 0.1 µm.
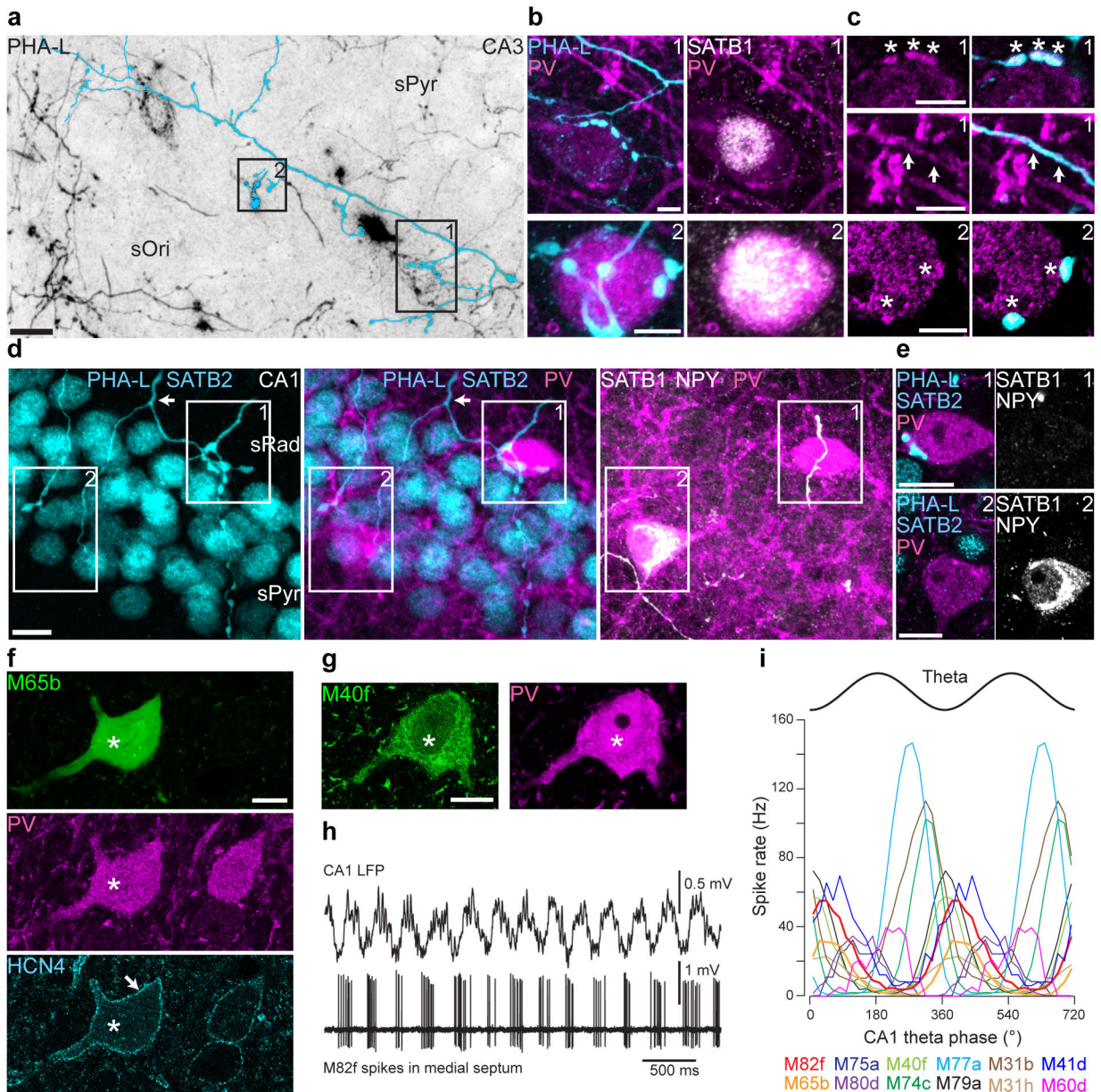
Supplementary Figure 5. Preferential targets of septo-hippocampal neurons and firing patterns of medial septal cells. (**a**) Digital trace (cyan) of a PHA-L-labeled septal axon preferentially targeting SATB1+/PV+ interneurons (unconnected PHA-L+ axons are black). (**b**) Left, septal-innervated PV+ somata from boxes 1 and 2 in **a**. Right, SATB1+ nuclei of same cells. (**c**) Single optical sections of parvalbumin-immunoreactivity from **b** shown with and without PHA-L-immunoreactivity. PV+ septal boutons, asterisks; main axon, arrows.

Supplementary Figure 5 (continued). (**d**) PHA-L-labeled septal axon (cyan, arrow) targeting a SATB1–/PV+ soma (magenta, in box 2) amongst SATB2+ CA1 pyramidal cells (cyan, nuclei). Another PV+ cell (in box 1), is SATB1+ and NPY+ (both white, nucleus and Golgi apparatus, respectively) and not innervated by the septal axon. Note NPY+ axons (white, e.g. inside boxed regions). (**e**) Single optical sections of both PV+ cells (from boxes 1 and 2 in **d**). Immunoreactivity for parvalbumin and PHA-L/SATB2 (left), and SATB1 and NPY (right). The septal innervated cell (from box 1) is SATB1– and NPY–. (**f** and **g**) Single optical sections of *in vivo* recorded neurobiotin-labeled medial septal cells M65b (**f**) and M40f (**g**). Parvalbumin, magenta; HCN4, cyan; asterisks, somata; arrow, plasma membrane. (**h**) Firing patterns of cell M82f (see Figure 7) during theta oscillations recorded in CA1. (**i**) Firing rate versus CA1 theta phase for medial septal cells. Same color code as in Fig. 7e and those identified with axons projecting to CA3 are shown with thick lines. Confocal z-stacks (number of optical sections / thickness in µm / intensity projection mode): **a**, 73/29/average (montage); **b** box 1, 52/15/average; box 2, 83/24/average; **d**, 84/32/average. Scale bars (µm): **a**, 20; **b**, **c**, **e**, 5; **d**, **f**, **g**, 10.
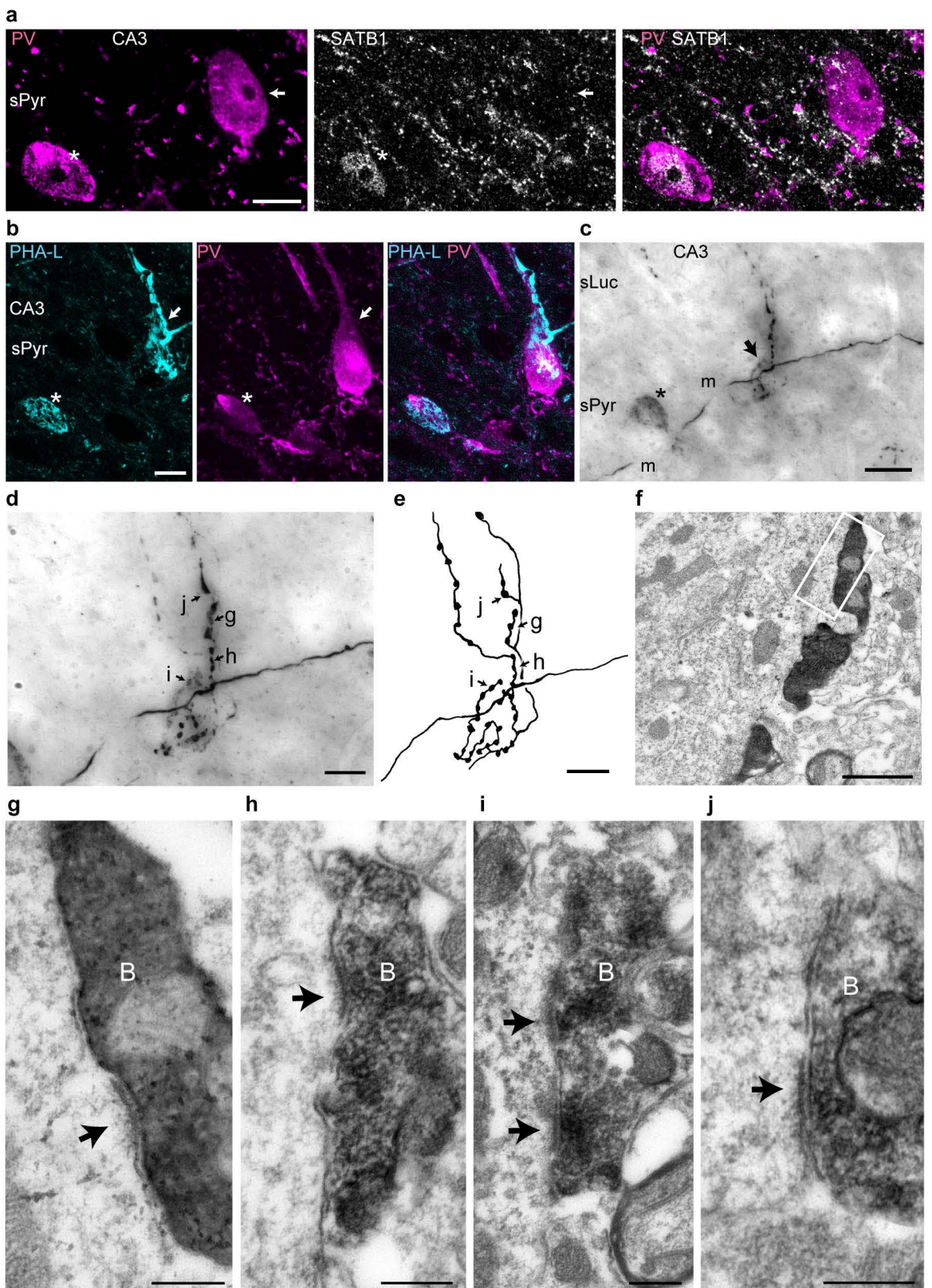
Supplementary Figure 6. Synapses between medial septal terminals and an axo-axonic cell identified by SATB1–/PV+ labeling.

Supplementary Figure 6 (continued). (**a**) Median-filtered confocal z-projection of parvalbumin-immunoreactivity (magenta) in two CA3 neurons. One neuron (asterisk) shows nuclear SATB1 immunoreactivity (white), the other has no detectable SATB1 immunoreactivity (arrow). (**b**) Confocal z-projection of PHA-L-labeled boutons (cyan) apposed to the PV+ (magenta) SATB1–immunonegative neuron shown in **a** (arrow). The PV+/SATB1+ neuron in **a** is not innervated by PHA-L boutons (asterisk). Both cells contain endogenous biotin (cyan, somatic labeling) that is visualized by the streptavidin-conjugated Alexa Fluor secondary antibody bound to the biotinylated anti-PHA-L primary antibody. (**c**) Light microscopic image z-stack of the same area after converting PHAL-immunoreactivity to diaminobenzidine-based HRP reaction product (20X objective), showing PHA-L-innervated SATB1–/PV+ cell from **a/b** (arrow) revealing axon (partially myelinated, m) bypassing the SATB1+/PV+ cell (asterisk). Note endogenous biotin in the soma. (**d**) Light microscopic z-stack image of PHA-L-innervated cell (100X objective). (**e**) Two-dimensional reconstruction of the medial septal-innervated cell. Four boutons in **d** and **e** (marked **g–j**) correspond to the panels below. (**f**) Electron micrograph of PHA-L-labeled boutons apposed to the target cell. Boxed region is shown rotated in **g**. (**g–j**) Synaptic junctions (arrows) between PHA-L-labeled septal boutons (B) and the target AAC. Confocal z-stacks (number of optical sections / thickness in μm / intensity projection mode): **a**, 2 separate single optical z-sections in same x-y location superimposed / 1.1 / maximum; **b**, 9 (PHA-L) and 27 (parvalbumin) optical sections superimposed / 15.1 / maximum; **c**, 24 / 13.7 / minimum; **d**, 93 / 24.2 / minimum. Scale bars: **a–b**, **d–e**, 10 μm; **c**, 20 μm; **f**, 1 μm; **g–j**, 0.2 μm.

Identified medial septal neuron		M82f	M65b	M75a	M80d	M40f
Immunohistochemical test	Parvalbumin	+s	+ds	+d	+ad	+s
	SATB1		+n	+n	+n	+n
	HCN4	+ds	+ds	+s	+ds	
	Calretinin					−s
	VGAT	+a		+a	+a	
	NECAB 1	−d	−d	−d	−d	
	Calbindin				−ds	
	Kv1.1			−s	+s	
	Target of projection axon	CA3	CA3	Dorsal fornix	Dorsal fornix*	na
***In vivo* firing patterns**	CA1 SWRs — Rate during SWRs (Hz)	23.4	17.2	7.3	27.9	43.9
	CA1 SWRs — Rate peri-SWR (Hz)	5.5	8.0	3.8	5.5	20.6
	CA1 SWRs — Mann-Whitney U comparison (P value, α = 0.05)	10^{-10}	8×10^{-7}	0.002	4×10^{-37}	2×10^{-10}
	CA1 SWRs — n (active)	27 (21)	34 (28)	33 (18)	68 (58)	57 (51)
	Theta firing rate (Hz)	23.1	11.7	12.8	13.4	20.0
	Theta coupling — Mean phase CA1 (°)	49.8	56.2	144.1	129.9	20.8
	Theta coupling — Mean vector length CA1	0.55	0.67	0.58	0.68	0.69
	Theta coupling — Rayleigh test P value (number of spikes)	$<10^{-100}$ (5434)	$<10^{-100}$ (4024)	4×10^{-16} (95)	4×10^{-54} (233)	$<10^{-100}$ (4074)
	Theta coupling — Mean action potentials per cycle	6.0	2.7	3.5	3.5	5.2
	Theta coupling — Active cycles (%)	99.1	96.5	93.1	94.4	98.7

Supplementary Table 1a.

Medial septal neuron (unlabeled)			M74c	M77a	M79a	M31b	M31h	M41d	M60d
In vivo firing patterns	CA1 SWRs	Rate during SWRs (Hz)	23.0	36.5	18.0	35.3	65.2	30.6	13.7
		Rate peri-SWR (Hz)	10.6	15.7	8.4	4.3	39.0	14.1	8.9
		Mann-Whitney U comparison (P value, α = 0.05)	10^{-5}	4×10^{-5}	3×10^{-8}	9×10^{-33}	4×10^{-5}	0.003	0.002
		n (active)	49 (34)	59 (42)	60 (45)	45 (38)	31 (31)	22 (17)	47 (33)
	Theta firing rate (Hz)		28.9	49.5	24.1	11.4	46.9	31.8	14.2
	Theta coupling	Mean phase CA1 (°)	318.3	269.9	14.8	32.9	302.7	71.0	207.3
		Mean vector length CA1	0.76	0.73	0.68	0.46	0.56	0.46	0.65
		Rayleigh test P value (number of spikes)	$<10^{-100}$ (8942)	$<10^{-100}$ (32364)	$<10^{-100}$ (8339)	$<10^{-100}$ (4370)	$<10^{-100}$ (3761)	2×10^{-33} (330)	8×10^{-24} (113)
		Mean action potentials per cycle	7.3	10.0	5.4	3.4	12.4	7.9	3.8
		Active cycles (%)	99.1	99.8	99.6	90.6	99.0	95.5	96.8

Supplementary Table 1b.

Supplementary Table 1 (a and b). Properties of sharp-wave-activated medial septal neurons. (+,–) indicates positive and negative immunoreactivity, respectively. Measurement location: s, soma; n, nucleus; d, dendrites; a, axons; na, not available. *Minor branches observed in medial CA1 and in subiculum.

Molecule	Host	Dilution and concentration (µg/ml)	Source	Code
Ankyrin-G	mouse	1:500, 1000	1	75-146, clone N106/36 (lot 441-4BK-91B)
Bassoon	mouse	1:500, 950	2	VAM-PS003, clone SAP7F407 (lot 901438)
Bassoon	guinea pig	1:500, antiserum	3	141004 (lot 3)
Calbindin	rabbit	1:5000, antiserum	4	CB-38 (lot 5.5)
Calretinin	rabbit	1:1000, antiserum	4	7699/3H (lot 18299)
ErbB4	mouse	1:1000, 200	5	MS-270-P, clone H4.77.16, same as Ab77
GABAAα1	rabbit	1:1000, 592	6	(Feb 2001 gift)
GABAAα1	guinea pig	1:300, 244	7*	(June 2011 gift)
Gephyrin	mouse	1:500, hybridoma supernatant	3	147 021 (lot 5), clone mAb7a/GlyR7a
Gephyrin	mouse	1:1000, 100	3	147 011 (lot 25)
Hyperpolarization-activated cyclic nucleotide-gated potassium channel 4 (HCN4)	mouse	1:500, 1000	1	clone N114/10 (lot 441-4BK-95Aa)
Kv1.1	mouse	1:1000, 1000	1	clone K36/15 (lot 440-5HK-57)
Metabotropic glutamate receptor 2/3 (mGluR2/3)	guinea pig	1:200, antiserum	7	(Feb 1996 gift)
Metabotropic glutamate receptor type 7b (mGluR7b)	guinea pig	1:2000, 830	7	K74 (Sept 2000 gift)
Neuronal Ca^{2+}-binding protein 1 (NECAB 1)	mouse	1:500, 500	8	H00064168-B01P (lot 09015 WUIZ)
Neuronal nitrogen oxide synthase (nNOS)	rabbit	1:1000, antiserum	9	AB5380 (lot 0507004069)
Neuropeptide Y (NPY)	sheep	1:700, antiserum	9	AB1583 (lot 25050288)

Molecule	Host	Dilution	Note	Catalog/ID
Neuropeptide Y (NPY)	rabbit	1:5000, antiserum	10	22940 (lot 208001)
Parvalbumin	guinea pig	1:5000, antiserum	3	195 004 (lot 5)
Parvalbumin	mouse	1:5000, ascites	4	235 (lot 10-11 F)
Parvalbumin	rabbit	1:500, antiserum	4	PV-28 (lot 5.5)
Parvalbumin	goat	1:2000, antiserum	4	PVG-214 (lot 3.6)
PHA-L	goat	1:5000, 2000	11	AS-2224 (lot T0817)
PHA-L	rabbit	1:500, 2000	11	AS-2300 (lot Q0205)
PHA-L-biotinylated	goat	1:1000, 1000	11	BA-0224 (lot M0724)
Pro-cholecystokinin	rabbit	1:500, 250	12	(April 2005 gift)
SATB1 (N-14)	goat	1:400, 200	13	sc-5989
SATB1 (N-14)	rabbit	1:1000, 1000	14	ab70004
SATB2	rabbit	1:1000, 100	14	ab34735
SATB2 (SATBA4B10)	mouse	1:200, 100	14	ab51502
Somatostatin (SOM)	mouse	1:200, 140	15	gtx71935, clone SOM-018
Vasoactive intestinal polypeptide (VIP)	rabbit	1:500, 1000	16	9535-0204 (lot 0109)
Vesicular GABA transporter (VGAT)	guinea pig	1:500, antiserum	3	131 004
Vesicular GABA transporter (VGAT)	rabbit	1:500, 600	12	Af500 (July 2003 gift)
Vesicular GABA transporter (VGAT)	rabbit	1:500, 1000	3	131 003 (lot 21)

Molecule (repeated)	Host	Epitope	Specificity test	Notes
Ankyrin-G	mouse	Monoclonal, fusion protein aa 990–2622, human Ankyrin-G.	No signal in knockout. Western blot; band at 270 kDa. Mouse cerebellar knockout: Zhou et al. (*The Journal of Cell Biology*, 1998, **143**, 1295–1599). Characterization: Jenkins and Bennett (*The Journal of Cell Biology*, 2001, **155**, 739–785).	a

Bassoon	mouse	Monoclonal, GST fusion protein aa 738–1035, rat bassoon.	Western blot; band at 420 kDa. Additional 350 kDa band and lower bands corresponding to putative proteolytic degradation products. Antibody generation and characterization: tom Dieck et al. (*The Journal of Cell Biology*, 1998, **142**, 499–1008).
Bassoon	guinea pig	Polyclonal, recombinant protein 330 C-terminal aa, rat bassoon.	Similar to mouse bassoon.
Calbindin	rabbit	Polyclonal, recombinant rat calbindin D-28k.	No signal in knockout. Mouse knockout: Airaksinen et al. (*Proceedings of the National Academy of Sciences*, 1997, **94**, 1488–1581). Characterization in rat hippocampus: Sloviter (*The Journal of Comparative Neurology*, 1989, **280**, 183–279).
Calretinin	rabbit	Polyclonal, recombinant human calretinin containing a 6-his tagged N-terminus.	Western blot supplied by Swant. No signal in knockout animals; Swant; Schiffmann et al. (*Proceedings of the National Academy of Sciences*, 1999, **96**, 5257–5262).
ErbB4	mouse	Monoclonal, extracellular fragment, recombinant human c-erbB-4/HER-4 oncoprotein.	No signal in knockout. Western blot; band as expected. Cross-species comparisons: Neddens et al. (*Biological Psychiatry*, 2011, **70**, 636–681). Antibody generation: Vullhorst et al. (*The Journal of Neuroscience*, 2009, **29**, 12255–12319), Chen et al. (*Journal of Biological Chemistry*, 1996, **271**, 7620–7629).
GABAAα1	rabbit	Polyclonal, N-terminal aa 1–9 (the extracellular side).	Same epitope, production, and labeling as rabbit GABAAα1 characterized in Baude et al. (*Cerebral Cortex*, 2007, **17**, 2094–2107), including mouse knockout test).
GABAAα1	guinea pig	Fusion protein, amino acids 328–382, mouse α1 subunit.	Western blot; band as expected. Tested in a knockout and in cells transfected with GABAAα1 cDNA. Characterization: Kaufmann et al. (*The Journal of*

			Comparative Neurology, 2009, **515**, 215–245).
Gephyrin	mouse	Monoclonal, N-terminus, rat gephyrin.	Western blot; band at 93 kDa. No Geph7a signal in knockout. Co-purifies with glycine receptor. Mouse knockout: Feng et al. 1998. Antibody generation: Pfeiffer et al. (*Proceedings of the National Academy of Sciences*, 1984, **81**, 7224–7231)..
Gephyrin	mouse	Monoclonal, N-terminus, rat gephyrin.	Same as Synaptic Systems 147 021 but purified IgG.
Hyperpolarization-activated cyclic nucleotide-gated potassium channel 4 (HCN4)	mouse	Monoclonal, fusion protein aa 1019–1108, rat HCN4, cytoplasmic domain.	Western blot, Khurana et al. (*The Journal of Neuroscience*, 2012, **32**, 2814–2823); Western blot and coimmunprecipitation, demonstration of preabsorbtion by HCN4 peptide, Partida et al. (*Investigative Ophthalmology & Visual Science*, 2012, **53**, 1696–1703); same 137kD band western blot as a polyclonal antibody, Stradleigh et al. (*The Journal of Comparative Neurology*, 2011, **519**, 2546–2573).
Kv1.1	mouse	Monoclonal, synthetic peptide aa 191–208, rat Kv1.1, extracellular domain.	No signal in knockout, Lorincz and Nusser (*The Journal of Neuroscience*, 2008, **28**, 14329–14340). Recognizes some somata as well as AISs, Lorincz and Nusser 2008, Campanac et al. (*Neuron*, 2013, **77**, 712–722). Also characterized by NeuroMab.
Metabotropic glutamate receptor 2/3 (mGluR2/3)	guinea pig	Polyclonal, intracellular C-terminal aa 813–872, rat mGluR2.	Recognizes mGluR2 and mGluR3 (transfected cell lines, Western blots, preabsorption). Generation and characterization of rabbit antibody H12: Ohishi et al. (*Neuron*, 1994, **13**, 55–121) and Shigemoto et al. (*The Journal of Neuroscience*, 1997, **17**, 7503–7525).
Metabotropic glutamate receptor type 7b (mGluR7b)	guinea pig	Polyclonal, synthetic peptide, C-terminal, human mGluR7b.	Western blot; 2 bands as expected. Abolished by preadsorption. No cross-reactivity with mGluR7a. Generation and characterization: Shigemoto et al. (*The Journal of Neuroscience*, 1997, **17**, 7503–7525).
Neuronal Ca^{2+}-binding protein 1 (NECAB 1)	mouse	Polyclonal, full-length human NECAB 1.	Same as in mouse. Western blots; as expected, no cross-reactivity with NECABs 2 and 3. Mouse brain, and antibody generation: Sugita et al. (*Neuroscience*,

			2002, **112**, 51–114).	
Neuronal nitrogen oxide synthase (nNOS)	rabbit	Polyclonal, recombinant human nNOS.	Does not cross react with iNOS or eNOS. No signal in knockout for rabbit antibody (Zymed/Invitrogen) of same mass. Mouse knockout and similar rabbit antibody: Gyurko et al. (*Endocrinology*, 2002, **143**, 2767–2841).	
Neuropeptide Y (NPY)	sheep	Polyclonal, synthetic peptide conjugated to bovine thyroglobulin.	Radioimmunoassays with other peptides lacked significant cross-reactivity except peptide YY. Antibody generation: Blessing et al. (*The Journal of Comparative Neurology*, 1986, **248**, 285–585).	b
Neuropeptide Y (NPY)	rabbit	Polyclonal, synthetic porcine NPY conjugated to methylated bovine serum albumin.	No significant cross-reactivity with other related peptides (APP, PYY). Antibody generation and characterization: Allen et al. (*Science*, 1983, **221**, 877–886).	c
Parvalbumin	guinea pig	Polyclonal, full length rat parvalbumin.	Western blot; abolished by pre-absorption with recombinant parvalbumin. Same labeling as Synaptic Systems rabbit antibody 195 002 and Swant monoclonal antibody 235. Rat hippocampus: Kosaka et al. (*Brain Research*, 1987, **419**, 119–149), Sloviter (*The Journal of Comparative Neurology*, 1989, **280**, 183–279). Mouse knockout: Schwaller et al. (*The American Journal of Physiology*, 1999, **276**, 403).	
Parvalbumin	mouse	Monoclonal, carp muscle parvalbumin.	No signal in knockout. Similar to other parvalbumin antibodies. Characterization: Celio et al. (*Cell Calcium*, 1988, **9**, 81–87). Mouse knockout: Schwaller et al. (*The American Journal of Physiology*, 1999, **276**, 403).	
Parvalbumin	rabbit	Polyclonal, purified parvalbumin, rat testis.	No signal in knockout, shown by Swant. Similar to other parvalbumin antibodies. Mouse knockout: Schwaller et al. (*The American Journal of Physiology*, 1999, **276**, 403).	
Parvalbumin	goat	Polyclonal, rat muscle	No signal in knockout, shown by Swant. Similar to	

		parvalbumin.	other parvalbumin antibodies. Mouse knockout: Schwaller et al. (*The American Journal of Physiology*, 1999, **276**, 403).	
PHA-L	goat	Raised to pure lectins in hyperimmunized goats.	Reacts with both Phaseolus vulgaris erythroagglutinin (PHA-E) and leucoagglutinin (PHA-L).	
PHA-L	rabbit	Raised to pure lectins in hyperimmunized goats.	Reacts with both Phaseolus vulgaris erythroagglutinin (PHA-E) and leucoagglutinin (PHA-L).	
PHA-L-biotinylated	goat	Raised to pure lectins in hyperimmunized goats.	Reacts with both Phaseolus vulgaris erythroagglutinin (PHA-E) and leucoagglutinin (PHA-L).	
Pro-cholecystokinin	rabbit	Cysteine-tagged C-terminal aa (CSAEDYEYPS), pro-cholecystokinin coupled to keyhole limpet hemocyanin.	Similar labeling to two non-commercial antibodies characterized by Sloviter and Nilaver (*The Journal of Comparative Neurology*, 1987, **256**, 42–102), Morino et al. (*The European Journal of Neuroscience*, 1994, **6**, 681–773).	
SATB1 (N-14)	goat	Polyclonal, N-terminus, human SATB1.	Similar labeling to rabbit antibody ab70004. Mouse cortex: Huang et al. (*Neuroscience Research*, 2011, **71**, 12–33). Mouse knockout: Balamotis et al. (*Molecular and Cellular Biology*, 2012, **32**, 333–380).	d
SATB1 (N-14)	rabbit	Polyclonal, 18 aa near N-terminus, human SATB1.	No signal in knockout for a similar rabbit antibody. Western blot, different band to SATB2 at mouse P1. Neuron-specificity shown by NeuN colocalization. Original rabbit antibody: Dickinson et al. (*Cell*, 1992, **70**, 631–1276). Mouse cortex: Huang et al. (*Neuroscience Research*, 2011, **71**, 12–33). Mouse knockout: Balamotis et al. (*Molecular and Cellular Biology*, 2012, **32**, 333–380).	e
SATB2	rabbit	Polyclonal, synthetic peptide conjugated to keyhole limpet	Same labeling as a non-commercial specific rabbit antibody that shows no cross-reactivity to SATB1 in mice; Western blot, double immunofluorescence tests.	f

		hemocyanin, aa 700 to C-terminus, mouse SATB2.	Isolation from rat cortex: Szemes et al. (*Neurochemical Research*, 2006, **31**, 237–283). Non-commercial SATB2: Balamotis et al. (*Molecular and Cellular Biology*, 2012, **32**, 333–380). Mouse brain: Britanova et al. *The European Journal of Neuroscience*, 2005, **21**, 658–726).	
SATB2 (SATBA4B10)	mouse	Monoclonal, recombinant fragment C-terminal, human SATB2.	Same CA1 pyramid nuclear immunoreactivity as rabbit antibody ab34735 but with additional labeling as observed for SATB1. Adult mouse brain: Nielsen et al. (*Cerebral Cortex*, 2010, **20**, 1904–1918; Fig. 1e). Mouse knockouts: Britanova et al. (*American Journal of Human Genetics*, 2006, **79**, 668–746), Dobreva et al. (*Cell*, 2006, **125**, 971–1057).	g
Somatostatin (SOM)	mouse	Monoclonal, conjugated to a protein carrier, human somatostatin.	Same labeling as a rat antibody Chemicon MAB354. No signal in preabsorption test for rat antibody. Mouse hippocampus, rat antibody: Jinno and Kosaka (*The Journal of Comparative Neurology*, 2000, **428**, 377–465). Rat antibody test: Kubota et al. (*Cerebral Cortex*, 2011, **21**, 1803–1820).	h
Vasoactive intestinal polypeptide (VIP)	rabbit	Polyclonal, synthetic peptide, full-length mature human VIP conjugated to keyhole limpet haemocyanin.	Similar labeling to 3 other VIP antibodies raised in rabbit against porcine VIP: Sloviter and Nilaver (*The Journal of Comparative Neurology*, 1987, **256**, 42–102).	
Vesicular GABA transporter (VGAT)	guinea pig	Polyclonal, Strep-Tag fusion protein, aa 2–115, rat VGAT (cytoplasmic domain).	Similar to C- and N-terminal fusion protein antibodies. Former gave additional unknown lower mass band in brain extract but same immunoreactivity as specific latter antibody; see rat cortex: Chaudhry et al. (*The Journal of Neuroscience*, 1988, **18**, 9733–9783). Similar rabbit antibody generation: Takamori et al. (*The Journal of Neuroscience*, 2000, **20**, 4904–4915).	
Vesicular GABA transporter	rabbit	Polyclonal, aa 31–112, mouse VGAT	Western blot; band at 57 kDa. Similar to guinea pig antibody. Characterization: Fukudome et al. (*The	

(VGAT)		(cytoplasmic domain).	*European Journal of Neuroscience*, 2004, **19**, 2682–2774).
Vesicular GABA transporter (VGAT)	rabbit	Polyclonal, synthetic peptide aa 75–87, rat VGAT (cytoplasmic domain) conjugated to keyhole limpet hemocyanin.	Same epitope and production as the specific VGAT/1 antibody by Takamori et al. (*The Journal of Neuroscience*, 2000, **20**, 4904–4915).

Supplementary Table 2. Primary antibodies. Notes: **a**, Observed in axon initial segments in CA3. Additional non-specific labeling occasionally observed in somata of CA3 sPyr. **b**, Weaker immunoreactivity in some interneurons in hippocampal sPyr compared to other NPY antibodies. Weak background in nuclei of neurons in sPyr. **c**, No significant background; strong immunoreactivity observed in subpopulations of hippocampal interneurons including in sPyr. **d**, At 1:100 dilution slight cross-reactivity detected with SATB2 (CA1 pyramidal cell nuclei). Weak immunoreactivity observed in CA4 neuron nuclei. **e**, Observed in hippocampal interneurons and not pyramidal neurons. Some interneurons that show strong immunoreactivity for the goat antibody sc-5989 are weak for the rabbit antibody. **f**, Observed in nuclei of CA1 pyramids and not interneurons. Cross-reactivity with blood vessels. **g**, Immunoreactivity observed in CA1 pyramidal cells and a subpopulation of interneurons, consistent with the combination of specific SATB2 and SATB1 antibodies. **h**, Labels same population of cells as other SOM antibodies but greater signal in dendrites and axon. List of sources: 1, UC Davis/NIH NeuroMab Facility, Davis, CA, USA. www.neuromab.org. 2, StressGen, via Bioquote Limited, York, UK. www.bioquote.com. Currently stocked by Enzo Life Sciences AG, Lausen, Switzerland. www.enzolifesciences.com. 3, Synaptic Systems Gesellschaft für neurobiologische Forschung, Entwicklung und Produktion mbH, Goettingen, Germany. www.sysy.com. 4, Swant, Bellinzona, Switzerland. www.swant.com. 5, Thermo Fisher Scientific, Kalamazoo, MI, USA. www.labvision.com. 6, Kind gift from Prof. W. Sieghart, Brain Research Institute, Vienna, Austria. 7, Kind gift from Prof. R. Shigemoto, Division of Cerebral Structure, National Institute for Physiological Sciences, Okazaki, Japan. 8, Abnova, Taipei City, Taiwan. www.abnova.com. 9, EMD Millipore Corporation, Billerica, MA, USA. www.millipore.com. 10, ImmunoStar, Inc. (DiaSorin), Hudson, WI, USA. www.immunostar.com. 11, Vector Laboratories, Inc., Burlingame, CA, USA. www.vectorlabs.com. 12, Kind gift from Professor M. Watanabe / FRONTIER INSTITUTE Co.Ltd, Hokkaido, Japan. http://www.frontier-institute.com. 13, Santa Cruz Biotechnology, Inc., Santa Cruz, CA, USA. www.scbt.com. 14, Abcam, Cambridge, UK. www.abcam.com. 15, GeneTex, Inc. Irvine, CA, USA. www.genetex.com. 16, MorphoSys UK Ltd t/a AbD Serotec, Oxford, UK. www.abdserotec.com. *Purified by Prof. W. Sieghart, Brain Research Institute, Vienna, Austria.